Particle Simulation Study on Tilt Stabilization in a FRC Plasma

Kazumi NISHIMURA

DOCTOR OF PHILOSOPHY

Department of Fusion Science
School of Mathematical and Physical Science
The Graduate University for Advanced Studies

1997 (School Year)

Contents

Abstract

The concept of a field-reversed configuration (FRC) is attractive for fusion plasmas because the magnetic configuration is very simple and a high beta plasma is confined inside the magnetic separatrix. The physics of FRC's has so far been studied from both theoretical and experimental points of view. An ideal MHD theory predicts that compact tori become unstable against an internal tilt mode. On the other hand, many experimental observations show that FRC plasmas remain stable much longer than the MHD growth time.

Until now, theoretical and numerical studies have examined various physical effects which have not been taken into account in an ideal MHD theory. They are roughly classified into the following three effects: (A) the finite ion Larmor radius effect, (B) the profile control effect, and (C) the ion beam effect. However, this contradiction remains unsolved up to the present. For example, the kinetic simulations with the particle orbit effect have disclosed that the tilt mode can be stabilized for a kinetic plasma of $\bar{s} \sim 1$ ($\bar{s}$: the dimensionless parameter associated with the ion Larmor radius), but it tends to be unstable for a moderately kinetic plasma of $2 \leq \bar{s} \leq 5$. On the other hand, in experiments, it is reported that the tilt mode is stable over a wide range of $\bar{s}$ ($1 < \bar{s} < 8$). This fact means that the tilt stability is not determined only by a single parameter $\bar{s}$. The numerical simulation by using an extended MHD model with Hall terms was carried out to verify

the profile control effect and found that a FRC with a hollow current profile becomes stable for a high enough separatrix beta value. In this model, however, $\bar{s}$ decreases as the current profile becomes hollow and the stable configuration is realized in kinetic plasmas of $\bar{s} \sim 1$. Therefore, this model cannot distinguish the profile control effect from the finite ion Larmor radius effect. In considering which of various effects is a key process leading to the tilt stabilization of FRC plasmas, it is important to develop the physical model which can control each effect independently and deal with them simultaneously. We carry out the three-dimensional macroscale electromagnetic particle simulation based on such a physical model.

We consider a FRC plasma confined by a uniform external magnetic field within a cylindrical conducting vessel. The plasma consists of thermal ions, thermal electrons, and cold beam ions which are treated as superparticles. The simulation starts from two-dimensional equilibrium. The temporal evolution of the system is given by solving both the equations of motion and the Maxwell equations in a self-consistent manner. In the present model, three kinds of parameters can be controlled independently. The first is the kinetic parameter $\bar{s}$ which controls the finite ion Larmor radius effect. The second are the profile control parameters β_{sp} and D which determine the pressure at the separatrix, and the hollowness of the current profile, respectively. The third are the number ratio of the beam ions to the thermal ions N_b/N_i, and the current ratio of the beam ions to the thermal plasma I_b/I_p, which control the ion beam effect. We carry out several simulation runs for a moderately kinetic plasma of $2 \leq \bar{s} \leq 5$ to clarify the tilt stabilization mechanism in this region. In the first place, we examine the dependences of tilt instability on both the finite ion Larmor radius effect and the profile control effect by carrying out several simulation runs with different values of β_{sp}, $\bar{s}$, and D. The result is that it is effective

against the tilt instability to increase the separatrix beta value (β_{sp}) and the tilt mode can be stabilized for a high β_{sp} (≥ 0.2). On the other hand, the stabilization of tilt mode can be scarcely altered by changing the $\bar{s}$ value and the current profile for low β_{sp} (≤ 0.1) and moderately kinetic plasmas. The detailed analysis reveals that the number flux of the ions crossing the magnetic separatrix repeatedly ("cycling ions") increases in proportion to β_{sp} and the tilt stability is realized for a large number flux of cycling ions.

The stabilization mechanism by cycling ions is as follows. Tilt instability is triggered by the internal mode, i.e., the collective motion of plasma is generated inside the magnetic separatrix. The typical cycling ions execute a gradient-$\boldsymbol{B}$ drift in the vicinity of the separatrix, and so they exist outside the separatrix as long as they do inside the separatrix on the average. The ions which make a cyclic motion across the separatrix are not able to follow the collective motion when they are moving outside the separatrix. The phase difference between the collective motions of cycling ions and non-cycling ions is created in proportion to the period during which cycling ions exist outside the separatrix. When cycling ions come back inside the separatrix, the internal tilting motion is disturbed by the motion of cycling ions. In other words, they play a role to suppress the tilting motion because their motion is out of phase with the tilting motion. The number of cycling ions increase as β_{sp} increase and thus the tilt mode is stabilized for a high β_{sp}. One can speculate that the cycling ions executing a gradient-$\boldsymbol{B}$ drift play a role as "chain" to connect the internal plasma with the external plasma and stabilize the tilting motion through their "chain" effect.

In the second place, we examine the dependences of tilt instability on the ion beam effect by carrying out two types of simulation runs. The first type is the case when the beam velocity varies while keeping the total number of beam ions for each run. The

second type is the case when the total number of beam ion varies while keeping the beam velocity for each run. For both cases, the growth rate remains almost unchanged until the current ratio I_b/I_p reaches the critical value of 0.03. However, the growth rate gradually decreases as the ratio increases above the critical value. The detailed examination reveals that this phenomena can be explained in terms of the effective $\bar{s}$ value, $\bar{s}_{eff}$, which is obtained by using the average velocity of all ions in place of the ion thermal velocity. The $\bar{s}_{eff}$ value is almost the same as $\bar{s}$ when $I_b/I_p < 0.03$. However, the derivation of $\bar{s}_{eff}$ from $\bar{s}$ becomes distinct for $I_b/I_p > 0.03$ and $\bar{s}_{eff}$ becomes smaller as I_b/I_p increases. We have the relation $\bar{s}_{eff} \sim 1$ for $I_b/I_p \sim 0.5$. It is concluded that the tilt stabilization by the energetic ion beam is realized for the small value of $\bar{s}_{eff}$. By comparing the above two cases, we examine the relation between the tilt growth rate and the kinetic energy ratio of total beam ions to total thermal plasma. In the case the velocity of beam ions varies, the ion beam needs 40% of the kinetic energy of thermal ions to reduce the growth rate below a half of that for the case without beam ions. On the other hand, in the case the total number of beam ions varies, only 10% of the kinetic energy of thermal ions is needed for the beam ions to get the same growth rate. Thus, the tilt mode can be suppressed more effectively by increasing the number ratio N_b/N_i.

Chapter 1

Introduction

1.1 Particle simulation study on tilt mode

1.1.1 Field-reversed configuration

The compact torus [1] is attractive for a fusion reactor because it has some superior features compared with the representative nominated reactor, e.g., tokamak. Since the diamagnetic toroidal current creates the poloidal magnetic field, it does not need the toroidal coil inherently, then the size of the compact torus reactor tends to be smaller. Furthermore, since there is no structure intersecting plasma torus, it is easy to transfer the plasma in the axial direction. A field-reversed configuration (FRC) is grouped into the compact tori. Figure 1.1 shows the magnetic field structure in a FRC plasma in the poloidal cross section. The toroidal current reverses the direction of the externally applied axial magnetic field in the vicinity of the structural symmetrical axis. Therefore, the magnetic field lines are divided into two types, i.e., open one and closed one. The dividing line represents the magnetic separatrix. Most of the plasma are mainly confined within the separatrix. FRC plasmas were observed experimentally at the first time by

Green [2] by using a field-reversed theta pinch method. This method is generally used to form the FRC plasma [3–6].

We begin with considering some of the characteristics of FRC plasmas in detail. There exist two kinds of field-null points in FRC's. One is what is called O-point (or field-null line) on the midplane. This singular point comes from two characteristic features, i.e., no toroidal field and reversal of the magnetic field. The other singular points exist on the z axis, so called X-point, in the vicinity of which particles execute the stochastic behavior [10]. Since the pressure of plasmas confined within the separatrix reaches its maximum value in the vicinity of the O-point, the averaged plasma beta $\langle\beta\rangle$ tends to be high in FRC plasmas ($\langle\beta\rangle \sim 1$). For the case of FRC's, β is defined by the ratio of the thermal pressure to the external magnetic pressure.

$$\beta \equiv \frac{P}{B_{ex}^2/8\pi} \tag{1.1}$$

It is well known in the two-dimensional model that the averaged β-value within the separatrix is approximately expressed by [7]

$$\langle\beta\rangle = 1 - \frac{1}{2}X_s^2 \,, \tag{1.2}$$

where X_s is the ratio of the separatrix radius to the radius of the conducting wall, which is defined on the midplane. This relation is derived under a few conditions, e.g., the conservation of magnetic flux between the midplane and the end region, and the pressure balance in axial and radial directions. The FRC plasma with high temperature can be sustained by the smaller external magnetic field than that of low β device, then this configuration is especially expected for a D-^{3}He fusion reactor [8,9]. In order to apply the FRC plasma to a fusion reactor, its features (e.g., stability, equilibrium, and confinement) should be investigated sufficiently.

The studies on FRC equilibria have been carried out from both theoretical analyses and experiments. MHD equilibrium solutions of FRC's can be derived from Grad-Shafranov equation in principle (see Section 2.2). The important point in solving the Grad-Shafranov equation is to determine the functional form of pressure profile [12–14] and the boundary condition [15–18]. Experimental observation showed many features of an equilibrium state of a FRC plasma, for example, the separatrix shape is elliptical, the density at the separatrix is $0.5 \sim 0.6$ of its maximum value at the field-null line, and the width of the plasma layer outside the separatrix is $2 \sim 6$ ion gyroradii [19]. Comparison between numerical solutions and experimental equilibria has also been carried out and good agreement is obtained [20]. A considerable number of studies have been made on the stability of FRC's. This thesis is focused on the tilt stabilization mechanism. The tilt instability predicted by the MHD theory has not been observed in the actual experiment. We will be able to understand the characteristics of the FRC plasma in detail through the research on the tilt stabilization mechanism.

1.1.2 Tilt instability

Many unstable modes in FRC plasmas have been predicted until now. Table 1.1 summarizes the features of the principal modes and whether or not they have been observed in experiments [11]. Our concern in this thesis is to examine the stabilization mechanism of the tilt mode, which is predicted to be unstable from the MHD analyses. The tilt mode is known as one of the most dangerous instabilities to disrupt the configuration completely. Although the analysis based on the ideal MHD theory predicts that the tilt mode will be unstable, many experimental observations show that FRC plasmas remain stable longer than the tilt growth time. Until now, various models with physical effects which are not

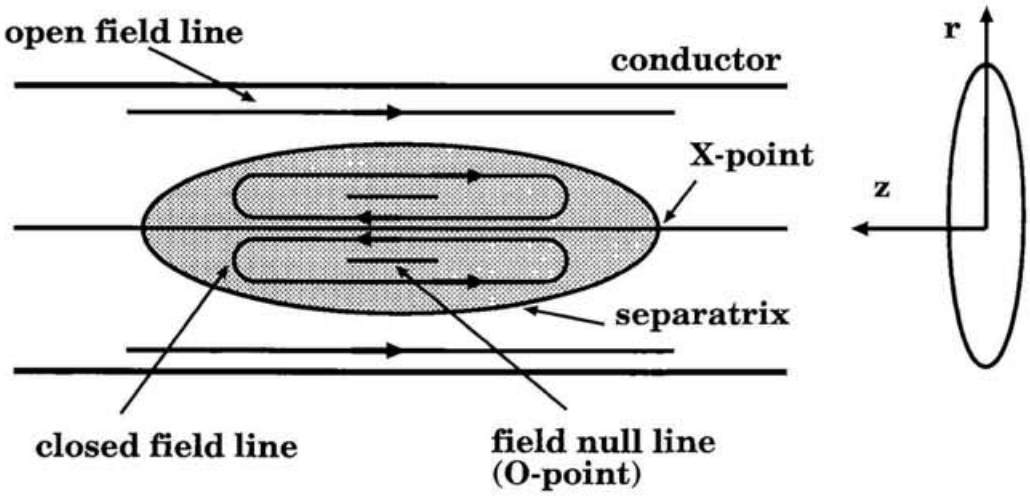

Figure 1.1: Magnetic field structure in a FRC

taken into account in an ideal MHD theory have been studied in order to explain this contradiction. The historical review of these models is described in Section 1.2. Many effects have been proposed, but none of them have given the satisfactory explanation as yet. There are many characteristic physical quantities in considering tilt stabilization, e.g., separatrix elongation, separatrix shape, ratio of the averaged ion Larmor radius to the separatrix radius, ratio of the separatrix radius to the conducting wall radius, pressure profile, averaged β-value, and so on. We cannot change only one quantity with keeping all the other quantities fixed because several quantities are complicatedly related to each other. Thus, in principle, it is impossible to extract only one of these effects without any influence of other effects.

We will examine the three effects (finite ion Larmor radius effect, profile control effect, and ion beam effect) in this thesis. Although these three effects has been investigated until now, it has not been indicated clearly whether each effect contributes to the tilt stabilization independently or the synergistic effect of these effects is of the essence. Although a large number of studies have been made on these effects, a complete conclusion is not obtained. In order to evaluate each effect, the physical model which can treat these three effects simultaneously and control them independently is needed (see Chapter 2). Furthermore, since the ion Larmor radius is not so small in FRC's compared with the confinement scale, the method based on the MHD theory seems to be unsuitable for describing the exact behavior of particles. In order to investigate the kinetic effects such as finite ion Larmor radius effect and ion beam effect, we carry out the three-dimensional electromagnetic particle simulation, in which the plasmas are treated as particles.

Table 1.1: FRC Stability: MHD theory versus experiment (from Table VI. in [11])

n (toroidal)	m (poloidal)	Mode character	Mode name	Experimental observation
Local ideal modes				
∞	0		Interchange	no
∞	1,2	Axial or radial	Co-interchange (ballooning)	no
Global ideal modes				
No rotation				
0	1	Axial	Roman candle	no
1	1	Radial	Sideway shift	no
≥ 1	1	Axial	Tilt	no
Rotation				
1	1	Radial	Wobble	yes[a]
2	1	Radial	$n = 2$	yes[b]
> 2	1	Radial	$n > 2$	no
Resistive modes				
0	2	Radial and axial	Tearing	yes[c]

[a] Saturates at finite amplitude.
[b] Stabilized by multipole fields.
[c] Disappeared in modern experiments.

1.2 Historical review of tilt instability

There are two dangerous modes in FRC plasmas which lead to the disruption of plasma confinement. One is the tilt mode ($n = 1, m = 1$) and another is the rotational mode ($n = 2, m = 1$), where n and m represent the toroidal and poloidal mode numbers, respectively. The rotational instability is observed experimentally [7]. This macroscopic instability caused by plasma rotation in the azimuthal (toroidal) direction results in elliptical deformation of the plasma density profile. The growth rate of this mode is the order of a reciprocal number of axial Alfvén transit time. The deformed plasma reaches the conducting wall in a final state. In the recent research, it is shown that rotational mode can be controlled by external multipole fields [21, 22] or injection of ion beams [23, 24]. Turning now to the tilt instability, we are confronted by the contradiction between theoretical studies and experimental observations. The analyses based on the MHD theory predict the growth time of tilt instability to be of the order of axial Alfvén transit time. However, this instability has not been observed in experiments.

Although a large number of studies have been made on tilt instability until now, the whole picture of tilt mode is not made clear completely. The purpose of this section is to provide a concise overview of historical studies and experiments of tilt instability in a FRC plasma.

1.2.1 Theoretical prediction

The study on the tilt instability has been brought to light by Bartoli and Green [25]. It has been observed in the theta pinch experiment that the plasma rotated around the axis orthogonal to the structural symmetrical axis. They first called the unstable phenomena

observed in the theta pinch flip instability. The point is that the plasma rotate around the axis orthogonal to the structural symmetrical axis. They approached this problem by treating it as a pure dynamics. That is to say, they replaced the plasma by the bar magnet laid in the opposite direction to the external magnetic field. But the situation is not so simple in real FRC plasmas.

MHD stability analysis for tilt mode in spheromak was first given by Rosenbluth and Bussac [26]. They investigated the stability of spheromak plasma at the minimum magnetic energy states under the constraint that the magnetic helicity K is invariant, where K is defined by

$$K = \int_V \boldsymbol{A} \cdot \boldsymbol{B} d^3\boldsymbol{r} \,, \tag{1.3}$$

where V represents the total volume of plasma, and $\boldsymbol{A}$ is the vector potential. They found that an internal tilt mode becomes unstable for a prolate configuration, but stable for an oblate one. There is no toroidal field in FRC, and hence no helical winding of magnetic field line exists, i.e., $K = 0$ in FRC. Furthermore, a FRC plasma is far from the minimum energy state what is called Taylor state [27] because high β plasmas are confined inside the magnetic separatrix. This means that their results is not applicable to the FRC plasma directly.

Clemente and Milovich [28] extended Rosenbluth and Bussac's theory to the FRC plasma. For a moment, let us look closely at their analysis. Hill's vortex solution is used for this study, in which the equilibrium is expressed in cylindrical coordinates (r, ϕ, z) by

$$\psi^0(r,z) = \pi B^0 r^2 \left(1 - \frac{r^2}{a^2} - \frac{z^2}{b^2}\right) \,, \tag{1.4}$$

$$P^0(r,z) = \frac{B^0}{8\pi^2}\left(\frac{1}{b^2} + \frac{4}{a^2}\right)\psi^0 \,, \tag{1.5}$$

$$\boldsymbol{B}^0(r,z) = -\frac{1}{2\pi r}(\boldsymbol{e}_\phi \times \nabla\psi^0) \,, \tag{1.6}$$

where $\psi^0(r,z)$, $P^0(r,z)$, and $\boldsymbol{B}^0(r,z)$ are the equilibrium quantities for poloidal magnetic flux, plasma pressure, and the magnetic field, respectively. B^0 is a constant which expresses the axial magnetic field at the separatrix on the midplane, and a and b are the radius and the half length of separatrix, respectively. Equation 1.4 indicates that the separatrix shape is elliptic. Let us discuss the stability of this equilibrium from the viewpoint of the energy principle. Denote the displacement vector by $\boldsymbol{\xi}$, then, the potential energy is given by [29]

$$\delta W = -\frac{1}{2}\int d^3\boldsymbol{r}\boldsymbol{\xi}\cdot\boldsymbol{F}\{\boldsymbol{\xi}\}, \tag{1.7}$$

$$\begin{aligned}\boldsymbol{F}\{\boldsymbol{\xi}\} &= \nabla(\boldsymbol{\xi}\cdot\nabla P^0 + \Gamma P^0\nabla\cdot\boldsymbol{\xi}) \\ &+ (\nabla\times\boldsymbol{B}^0)\times[\nabla\times(\boldsymbol{\xi}\times\boldsymbol{B}^0)] \\ &+ (\nabla\times[\nabla\times(\boldsymbol{\xi}\times\boldsymbol{B}^0)])\times\boldsymbol{B}^0,\end{aligned}$$

where Γ denotes the ratio of specific heats. If δW is negative, the system appears to be unstable [30]. Let us consider two interesting cases with different functional forms of $\boldsymbol{\xi}$. First, we assume the special divergence-free perturbation that induces a rotation of plasma around the axis $z=0$, $\phi=0,\pi$ without deformation of the separatrix,

$$\boldsymbol{\xi} = \epsilon\left(\boldsymbol{e}_r\frac{z}{b^2}\sin\phi + \boldsymbol{e}_\phi\frac{z}{b^2}\cos\phi - \boldsymbol{e}_z\frac{r}{a^2}\sin\phi\right), \tag{1.8}$$

where ϵ is an infinitesimal. That is to say, this means an internal displacement. By using this form of the displacement vector $\boldsymbol{\xi}$, we can obtain the expression of δW

$$\delta W = \frac{3\epsilon^2 B_0^2}{40b}\left(\frac{a^2}{b^2}-1\right). \tag{1.9}$$

This expression leads to the conclusion that the prolate FRC ($b>a$) is unstable to the tilt mode. Note that this conclusion is the same as that for a spheromak plasma. Second,

we assume the another perturbation $\boldsymbol{\xi}$,

$$\boldsymbol{\xi} = \epsilon(\boldsymbol{e}_r z \sin\phi + \boldsymbol{e}_\phi r \cos\phi - \boldsymbol{e}_z r \sin\phi). \tag{1.10}$$

This means the rigid rotation of a plasma around the axis $z = 0$, $\phi = 0, \pi$, i.e., an external displacement. It is straightforward to integrate the expression δW in this case and we can see it must be zero. Thus we arrive at the conclusion that the FRC plasma is stable to the external tilt motion. Clemente and Grillo [31] also investigated the same problem with using the Maschke-Hernegger solution and reached at the similar conclusion. On the other hand, Hammer [32] extended the Rosenbluth and Bussac's idea to the equilibrium with the arbitrary plasma pressure, but the nearly spherical separatrix shape. All these analyses are based on the ideal MHD theory and their common conclusion is that the internal tilt mode is always unstable in the prolate FRC plasma.

1.2.2 MHD simulation

The number of equilibrium solutions which can be treated analytically is limited and it is difficult to express concisely the actual configurations of experiments. Schwarzmeier *et al.* [33] investigated the numerical solutions of Grad-Shafranov equation. They adopted the hyperbolic tangent form as the pressure shape function and explored the equilibrium which reproduces the actual configurations of some experiments. Their result was that the equilibrium solution exists only in the limited region of the (X_s, β_{sp}) space. The notation X_s represents the ratio of the radius of the separatrix to the radius of the conducting confinement vessel r_D on the midplane, namely

$$X_s = r_{sp}/r_D \tag{1.11}$$

and β_{sp} means the normalized pressure value at the separatrix,

$$\beta_{sp} = P(r_{sp})/P_{max} \ , \tag{1.12}$$

where P_{max} is the maximum value of the pressure on the midplane. Furthermore, they used a time-dependent linearized MHD code [34] and investigated whether these equilibrium are stable against the tilt mode. Although the shape of separatrix of their solution changed variously from ellipse to racetrack-shape, it was found that all equilibrium are unstable to the internal tilt mode.

On the other hand, though the mode is linearly unstable, there is the possibility that the tilt amplitude may saturate at a low level due to the nonlinear effect in the framework of the ideal MHD model. Horiuchi and Sato [35] investigated this problem by means of a three-dimensional full magnetohydrodynamic simulation. They came to the conclusion that the internal tilt mode cannot stay at a low amplitude and leads to the disruption of the configurations except for a spinning plasma with a high velocity. At the same time, this study leads to the conclusion that the growth rate of the tilt mode for the uniform external field case is represented by

$$\gamma_M = C\frac{V_A}{Z_{sp}} \ , \tag{1.13}$$

where Z_{sp} is the separatrix half-length along the z axis, and V_A is the average Alfvén velocity associated with the volume-averaged magnetic field and the ion density at the field-null line. The coefficient C, which is of the order of unity, depends on the elongation of the magnetic separatrix.

Milroy *et al.* [36] also studied the nonlinear evolution of the tilt instability by using the three-dimensional resistive MHD code with the Hall effect. Their numerical studies indicated that the Hall term does not suppress the tilt mode effectively in the range of

the parameters used in most of experiments.

1.2.3 Finite ion Larmor radius effect

The finite ion Larmor radius effect is characterized by the kinetic parameter $\bar{s}$ [38] which is defined by

$$\bar{s} = \int_R^{r_{sp}} \frac{r dr}{r_{sp} \lambda_i}, \tag{1.14}$$

where r_{sp} is the separatrix radius, R is the radius of the field-null line, and λ_i is the local ion gyroradius at the midplane. Roughly speaking, this parameter indicates the ratio of the plasma radius to the ion Larmor radius.

Barnes *et al.* [39–42] evaluated numerically the finite ion Larmor radius effect by using a Vlasov-fluid theory, in which ions are treated as collisionless species and electrons are assumed to be cold and massless. By this research, they found that the tilt mode can be stabilized for a kinetic plasma of $\bar{s} \leq 2$, but it tends to be unstable for a moderately kinetic plasma of $2 \leq \bar{s} \leq 10$ and the growth rate increases as the $\bar{s}$-value increases. But it is necessary to note the following points [43]. First of all, although they used the finite Larmor radius model based on the assumption that the Larmor radius of ions are small everywhere compared with the confinement scale, the radii of ions in the vicinity of the field-null line become considerable large. Therefore, this theory is doubtful at the application to the FRC plasma. Secondly, the magnetic moment μ is not conserved at the tips of the flux surfaces in an equilibrium configuration under the experimentally realistic parameters, thus their numerical model with the assumption that μ is conserved is not able to explain the experimental results strictly.

In order to avoid these problems, Horiuchi and Sato [44] executed the particle simulation which treated both ions and electrons as particles. In their investigation, the concrete

orbits of ions are shown and the specific orbits across the field-null line, "meandering orbits," are discussed in detail. The number of particles which execute the meandering motion increases as the $\bar{s}$-value decreases. Since the results of this particle simulation indicate the tilt mode to be stable for a kinetic plasma of $\bar{s} < 2$, it seems reasonable to conclude that this specific behavior of ions contributes to the suppression of the tilt instability. But this simulation adopted the rigid rotor model in which average ion velocity along the azimuthal direction increases as the radial location moves outwards and $\bar{s}$ decreases, then, the stabilization by the ions with a high rotational velocity may be more efficient with decreasing $\bar{s}$.

1.2.4 Profile control effect

Steinhauer and Ishida [45] analyzed the experimental measurements of several devices and pointed out the correlation between current profile and X_s. To classify the current profiles, they introduced the current profile parameter h, which is defined by

$$h \equiv [(j_\phi/r)_{r=R}]/\langle j_\phi/r \rangle \ , \tag{1.15}$$

where j_ϕ is the toroidal current density and the average $\langle j_\phi/r \rangle$ is taken over the cross section inside the separatrix on the midplane. The equilibrium current profile with $h = 1$ denotes "flat" profile, $h < 1$ and $h > 1$ correspond to "hollow" and "peaked" profiles, respectively (See Fig.1 in Ref. [45]). The relation between the current profile parameter h and X_s was found to be expressed by

$$h \simeq 0.05 + 1.7 X_s \ . \tag{1.16}$$

Many experimental data show that the parameter X_s takes the value between 0.3 and 0.65, and the current profile parameter h exists between 0.5 and 1.0. That is, most

experimental equilibrium configurations tend to take the "hollow" current profile.

Cobb *et al.* [46] verified the profile stabilization of the tilt mode by the extended MHD simulation. In this study, they included the Hall term in the MHD equations and found that the equilibrium with "hollow" current profile is stable against the tilt mode if the beta value at the separatrix β_{sp} is enough large. In their model, however, $\bar{s}$ decreases as the current profile becomes hollow, and the stable configuration is realized in kinetic plasmas of $\bar{s} \sim 1$. Therefore, their model cannot distinguish the profile control effect from the finite ion Larmor radius effect or the Hall effect strictly. In addition, the effect of the separatrix shape has been discussed by Steinhauer *et al.* [47] and Kanno *et al.* [48]. Steinhauer *et al.* [47] suggested that the equilibrium which are stable to the tilt mode exists in the ideal MHD theory if the current profile is hollow and the separatrix shape is racetrackness. Kanno *et al.* [48] argued this idea in detail. Since the stable equilibrium measured in the experiments must always include the kinetic effects, it is difficult to ascertain this effect in actual experiments.

1.2.5 Plasma rotation effect

The rotation of a FRC plasma has been observed, and consequently it causes a rotational instability, where plasma rotates azimuthally while being suffering from the $n = 2$ profile deformation. This rotational instability was observed in many experiments actually, but it can be suppressed by applying multipole field in general. The origin of rotation itself remains unclear up to the present [49–51]. Clemente and Milovich [52] investigated the rotational effect in the tilt instability with a simple fluid model. Their result indicated that this effect does not appear to be significant in the stabilization of the tilt mode in a FRC since the measured angular velocities in the experiments are a factor of 5 lower

than required for the tilt stabilization by their analysis.

In order to illustrate this effect from the different point of view, the studies on the tilt stabilization by the beam injection into the unstable FRC plasma have been made. There have been many studies [53] on the stabilization of the MHD unstable system by injecting the energetic particles until now and the stabilizing effects actually have been observed in bumpy torus, mirror, and tokamak experiments. Finn and Sudan [54] summarized a review paper about the FRC with a component of energetic particles, in which a detailed discussion was given in terms of the energy principle. Nomura [55] studied this problem analytically with using the Hill's vortex solution and found that the tilt instability is suppressed if the circulation frequency of beam ions is close to the axial betatron frequency. But the beam current is assumed not to disturb the equilibrium configuration of background plasma in this analysis. On the other hand, Barnes and Milroy [56] investigated the same problem numerically. They used the three-dimensional code, in which the beam ion and the background plasma are treated as a particle and MHD fluid, respectively. The equations of motion of beam particles and the MHD equations are advanced in time self-consistently. The beam ions are injected gradually into the plasma at the initial equilibrium state, then the configuration of background plasma is changed markedly after a few Alfvén times. These simulation results lead to the conclusion that the tilt instability can be stabilized if kinetic energy of beam particles exceeds 40 % of the kinetic energies of both the total plasma and beam particles.

1.2.6 Experimental observation

Until now, the tilt instability has not been observed in most of experiments [57]. The parameter $\bar{s}$ in early experiments are estimated to be less than 2 ($\bar{s} < 2$). Therefore, this

fact suggests that the finite ion Larmor radius effect seems to suppress the tilt instability in these cases.

In recent years, one large experimental device was constructed, which is commonly called LSX (abbreviation of "large s experiment") [58,59], in which $\bar{s}$ can be changed over a wide range ($1 < \bar{s} < 8$) (see Table.1.2). In this device, it was expected that the tilt mode turns out to be unstable if $\bar{s}$ becomes greater than 2. It is generally difficult to diagnose the internal tilt mode because it does not cause the deformation of the separatrix. The problem is how to detect the evidence of the tilt instability. In the equilibrium state, there is no toroidal field B_ϕ in a FRC plasma, then one way to find the evidence of instability is to measure the toroidal components of magnetic field. An array of external B_ϕ pickup loops are used for this measurement [61, 62]. Since these probes are settled along the quartz tube, they cannot directly measure the field within the separatrix. They can sense only the distortions of the separatrix shape. The result of this experiment is that the tilt instability is seldom observed.

On the other hand, the result measured in the FRX-C/LSM (abbreviation of " field-reversed experiments-C / large source modification") device [63,64] shows the observations of internal tilt instability [62,65]. Since they also use an array of external B_ϕ pickup loops, they cannot measure the internal tilt mode in the strict sense of the word. Although they determined the limit of unstable region ($\bar{s}/E_0 < 0.2 \sim 0.3$ is a regime of gross stability, where $E_0 \equiv Z_{sp}/r_{sp}$ is the separatrix elongation), stable FRC's have been observed beyond this limit actually [58].

1.2.7 Purpose of this study

The purpose of this study is to make clear the whole story of the tilt stabilization in a FRC plasma. The following three effects are discussed in this study: (A) the finite ion Larmor radius effect, (B) the profile control effect, and (C) the ion beam effect. In a real plasma various effects appear simultaneously, which makes the phenomena complex. For example, let us consider a hollow current profile in which particles with a high velocity are localized near a magnetic separatrix. The finite ion Larmor radius effect creates the plasma leakage outside the separatrix and makes the pressure finite there. An electric field is also generated there due to the finite ion Larmor radius effect. The existence of a finite pressure at the separatrix and the electric field, in turn, alters an original equilibrium profile to the different one. In considering which of various effects is a key process leading to the tilt stabilization of FRC plasmas, it is important to develop the physical model which can control each effect independently and dealt with them simultaneously. We carry out the three-dimensional macroscale electromagnetic (EM) particle simulation based on such a physical model.

Table 1.2: Average FRC life-times and plasma conditions on LSX (From [59]).

Fill pressure (mTorr)	$1.25 \sim 20$
Liftoff flux (mWb)	$12 \sim 45$
Magnetic field (kG)	$4.3 \sim 7.7$
Separatrix radius (cm)	$15.0 \sim 21.5$
Separatrix length (cm)	$140 \sim 385$
Elongation	$4.7 \sim 9.0$
Electron density ($\times 10^{15}/cm^3$)	$1.1 \sim 3.5$
Electron temperature (eV)	$80 \sim 400$
Ion temperature (eV)	$80 \sim 900$
$X_s \equiv r_{sp}/r_D$	$0.33 \sim 0.48$
Poloidal flux (mWb)	$5.5 \sim 11$
$\bar{s}$-value	$1 \sim 8$
Flux life-time τ_ϕ (μs)	$115 \sim 490$
Particle life-time τ_N (μs)	$160 \sim 650$
Energy life-time τ_E (μs)	$90 \sim 300$

Chapter 2

Simulation model

In this chapter, we describe the model for the particle simulation in detail. This chapter is composed of four sections. First section is devoted to introduction of normalized basic equations, which are the equations of motion and the Maxwell equations. We consider the FRC plasma confined by a uniform external magnetic field within the cylindrical vessel. We use a MHD equilibrium solution with a beam component as an initial condition of particle simulation. The method how to obtain the equilibrium solution is described in second section. MHD equilibrium solution without a beam component can be given by solving the Grad-Shafranov equation. Because we consider the three component plasma (thermal ion, thermal electron, and beam ion), the method to get the equilibrium solution becomes more complicated. The boundary condition for the particles and the field quantities are described in third section. The fourth section is devoted to the discussion of the numerical scheme used for particle simulation.

2.1 Basic equations

2.1.1 Normalized equations

The equations to be solved are the equations of motion

$$\frac{d(\gamma_j \boldsymbol{v}_j)}{dt} = \frac{q_j}{m_j}[\boldsymbol{E} + \frac{\boldsymbol{v}_j}{c} \times \boldsymbol{B}] , \tag{2.1}$$

$$\frac{d\boldsymbol{x}_j}{dt} = \boldsymbol{v}_j , \tag{2.2}$$

and the Maxwell equations

$$\frac{1}{c}\frac{\partial \boldsymbol{B}}{\partial t} = -\nabla \times \boldsymbol{E} , \tag{2.3}$$

$$\frac{1}{c}\frac{\partial \boldsymbol{E}}{\partial t} = \nabla \times \boldsymbol{B} - 4\pi \boldsymbol{j} , \tag{2.4}$$

$$\nabla \cdot \boldsymbol{E} = 4\pi\rho , \tag{2.5}$$

where $\boldsymbol{x}_j(t), \boldsymbol{v}_j(t)$, m_j and q_j are the position, the velocity, the rest mass and the charge of the j-th particle, c is the light velocity in vacuum, and the relativistic γ-factor of the j-th particle is defined by

$$\gamma_j = 1/\sqrt{1 - (\boldsymbol{v}_j \cdot \boldsymbol{v}_j)/c^2} . \tag{2.6}$$

The current density $\boldsymbol{j}(\boldsymbol{x}, t)$ and the charge density $\rho(\boldsymbol{x}, t)$ are obtained by summing over all the particles, namely,

$$\boldsymbol{j}(\boldsymbol{x}, t) = \sum_{j=1}^{N_{tot}} \frac{q_j \boldsymbol{v}_j(t)}{c} S[\boldsymbol{x} - \boldsymbol{x}_j(t)] , \tag{2.7}$$

$$\rho(\boldsymbol{x}, t) = \sum_{j=1}^{N_{tot}} q_j \, S[\boldsymbol{x} - \boldsymbol{x}_j(t)] , \tag{2.8}$$

where N_{tot} is the total number of particles and $S(\boldsymbol{x})$ is the form function [67] of particles which are expressed by a triangle with the base length equal to 2.0 times the grid separation [68]. The detailed explanation of superparticle will be given in Section 2.4.

We have to express the basic equations (2.1)~(2.5) by dimensionless quantities in carrying out the numerical simulation. For this, we introduce the fundamental physical quantities as

$$\begin{aligned} charge &\Rightarrow q_N\ , \\ velocity &\Rightarrow c\ , \\ mass &\Rightarrow M_N\ , \\ field &\Rightarrow B_N\ , \end{aligned}$$

where B_N is the vacuum external magnetic field which confines the FRC plasma, q_N and M_N mean the charge and mass of superparticle electron, respectively. If one superparticle consists of N real electrons, the relations $q_N = Ne$ and $M_N = Nm_e$ hold, where e and m_e is the charge and mass of real electron, respectively.

By using these four quantities, we can constitute the units of time,

$$\frac{M_N c}{q_N B_N}\ (\equiv t_N) \tag{2.9}$$

and of length,

$$\frac{M_N c^2}{q_N B_N}\ (\equiv R_N)\ . \tag{2.10}$$

This means that we adopt the inverse of non-relativistic electron cyclotron frequency in the vacuum external magnetic field as a unit of time.

Let us normalize the equations of motion and Maxwell equations by using these units. (In the following equations, the tilde denotes the normalized quantities.)

$$\begin{aligned} \frac{d(\gamma_j \boldsymbol{v}_j)}{dt} &= \frac{q_j}{m_j}[\boldsymbol{E} + \frac{\boldsymbol{v}_j}{c}\times\boldsymbol{B}] \\ &\rightarrow \frac{c}{t_N}\frac{d(\tilde{\gamma}_j\tilde{\boldsymbol{v}}_j)}{d\tilde{t}} = \frac{q_N B_N}{M_N}\frac{\tilde{q}_j}{\tilde{m}_j}[\tilde{\boldsymbol{E}} + \tilde{\boldsymbol{v}}_j\times\tilde{\boldsymbol{B}}] \end{aligned}$$

$$\rightarrow \quad \frac{d(\tilde{\gamma}_j \tilde{\boldsymbol{v}}_j)}{d\tilde{t}} = \frac{\tilde{q}_j}{\tilde{m}_j}[\tilde{\boldsymbol{E}} + \tilde{\boldsymbol{v}}_j \times \tilde{\boldsymbol{B}}] \,, \tag{2.11}$$

$$\begin{aligned}
\frac{d\boldsymbol{x}_j}{dt} &= \boldsymbol{v}_j \\
&\rightarrow \quad \frac{R_N}{t_N}\frac{d\tilde{\boldsymbol{x}}_j}{d\tilde{t}} = c\tilde{\boldsymbol{v}}_j \\
&\rightarrow \quad \frac{d\tilde{\boldsymbol{x}}_j}{d\tilde{t}} = \tilde{\boldsymbol{v}}_j \,, \qquad (2.12) \\
\frac{1}{c}\frac{\partial \boldsymbol{B}}{\partial t} &= -\nabla \times \boldsymbol{E} \\
&\rightarrow \quad \frac{1}{c}\frac{B_N}{t_N}\frac{\partial \tilde{\boldsymbol{B}}}{\partial \tilde{t}} = -\frac{B_N}{R_N}\tilde{\nabla} \times \tilde{\boldsymbol{E}} \\
&\rightarrow \quad \frac{\partial \tilde{\boldsymbol{B}}}{\partial \tilde{t}} = -\tilde{\nabla} \times \tilde{\boldsymbol{E}} \,, \qquad (2.13) \\
\frac{1}{c}\frac{\partial \boldsymbol{E}}{\partial t} &= \nabla \times \boldsymbol{B} - 4\pi \sum_{j=1}^{N} \frac{q_j \boldsymbol{v}_j(t)}{c} \; S[\boldsymbol{x} - \boldsymbol{x}_j(t)] \\
&\rightarrow \quad \frac{1}{c}\frac{B_N}{t_N}\frac{\partial \tilde{\boldsymbol{E}}}{\partial \tilde{t}} = \frac{B_N}{R_N}\tilde{\nabla} \times \tilde{\boldsymbol{B}} - \frac{4\pi}{c}\frac{q_N c}{R_N^3}\sum_{j=1}^{N} \tilde{q}_j \tilde{\boldsymbol{v}}_j S[\tilde{\boldsymbol{x}} - \tilde{\boldsymbol{x}}_j] \\
&\rightarrow \quad \frac{\partial \tilde{\boldsymbol{E}}}{\partial \tilde{t}} = \tilde{\nabla} \times \tilde{\boldsymbol{B}} - \frac{4\pi q_N}{B_N R_N^2}\sum_{j=1}^{N} \tilde{q}_j \tilde{\boldsymbol{v}}_j S[\tilde{\boldsymbol{x}} - \tilde{\boldsymbol{x}}_j] \\
&\rightarrow \quad \frac{\partial \tilde{\boldsymbol{E}}}{\partial \tilde{t}} = \tilde{\nabla} \times \tilde{\boldsymbol{B}} - C_J \tilde{\boldsymbol{j}} \,, \qquad (2.14) \\
\nabla \cdot \boldsymbol{E} &= 4\pi\rho(\boldsymbol{x}, t) \\
&\rightarrow \quad \frac{B_N}{R_N}\tilde{\nabla} \cdot \tilde{\boldsymbol{E}} = 4\pi \frac{q_N}{R_N^3}\sum_{j=1}^{N} \tilde{q}_j S[\tilde{\boldsymbol{x}} - \tilde{\boldsymbol{x}}_j] \\
&\rightarrow \quad \tilde{\nabla} \cdot \tilde{\boldsymbol{E}} = C_J \tilde{\rho} \,, \qquad (2.15)
\end{aligned}$$

where we define the coupling constant C_J as,

$$C_J \equiv \frac{4\pi q_N}{B_N R_N^2} \,. \tag{2.16}$$

2.2 Initial condition

2.2.1 Equilibrium solution of thermal plasmas

We consider the case when the FRC plasma is composed of three components, i.e., thermal ion, thermal electron, and beam ion and pursue the time development by means of three-dimensional particle simulation. It is necessary to determine the position and velocity of each particle, and electromagnetic fields as initial conditions for particle simulation. For this purpose, we use two-dimensional MHD equilibrium solution. In this subsection, we consider the MHD equilibrium of thermal plasma without beam component.

In the stationary state, each fluid equation of thermal ion and electron is given by

$$m_j n_j (\boldsymbol{V}_j \cdot \nabla)\boldsymbol{V}_j = -\nabla P_j + q_j n_j \left(\boldsymbol{E} + \frac{\boldsymbol{V}_j}{c} \times \boldsymbol{B} \right) \quad (j = i, e) \,, \tag{2.17}$$

where $\boldsymbol{V}$ and n represent the fluid velocity and the number density, respectively, and the subscripts i and e denote the quantities for ions and electrons, respectively. Let us assume that the ion flow is zero everywhere, $\boldsymbol{V}_i = 0$ because of large inertia ($m_i/m_e \gg 1$). This means that an electric current is carried only by electrons. Then the equation of ion fluid is reduced to

$$0 = -\nabla P_i + q_i n_i \boldsymbol{E} \,. \tag{2.18}$$

Let us evaluate the electron inertia term [left-hand side of Eq.(2.17)] roughly. We have two relations as

$$\frac{1}{m_e n_e} \nabla P_e \sim \frac{1}{L} v_{Te}^2 \,, \tag{2.19}$$

$$(\boldsymbol{V}_e \cdot \nabla)\boldsymbol{V}_e \sim \frac{1}{L} V_e^2 \,, \tag{2.20}$$

where L is the characteristic length of this system. If the electron fluid velocity is much

smaller than the electron thermal velocity, i.e.,

$$v_{Te} \gg V_e \,, \tag{2.21}$$

the electron inertia term can be neglected because the relation

$$|\nabla P_e| \gg m_e n_e \,|(\boldsymbol{V}_e \cdot \nabla)\boldsymbol{V}_e| \tag{2.22}$$

holds. Then, two fluid equations are reduced to,

$$-\nabla P_i + q_i n_i \boldsymbol{E} = 0 \,, \tag{2.23}$$

$$-\nabla P_e + q_e n_e \left(\boldsymbol{E} + \frac{1}{c}\boldsymbol{V}_e \times \boldsymbol{B}\right) = 0 \,. \tag{2.24}$$

By adding Eq.(2.23) to Eq.(2.24), the force balance equation for one fluid is given by

$$-\nabla(P_i + P_e) + (q_i n_i + q_e n_e)\boldsymbol{E} + \frac{1}{c} q_e n_e \boldsymbol{V}_e \times \boldsymbol{B} = 0 \,. \tag{2.25}$$

Here we introduce the diamagnetic current density,

$$\boldsymbol{j}_d \equiv q_e n_e \boldsymbol{V}_e \tag{2.26}$$

and the total pressure

$$P \equiv P_i + P_e \,. \tag{2.27}$$

Furthermore, we assume the quasineutrality of FRC plasmas, i.e.,

$$n_i \approx n_e \,. \tag{2.28}$$

After all, the following balance equation is obtained:

$$-\nabla P + \frac{1}{c}\boldsymbol{j}_d \times \boldsymbol{B} = 0 \,. \tag{2.29}$$

This equation is the usual MHD balance equation, then it is possible to obtain this relation directly from MHD equations. But we should notice the several assumptions introduced

in this process. These assumptions should be taken into account for determining the position and velocity of each particle later. We will obtain the equilibrium quantities (the toroidal current density, the magnetic field, and the pressure profile) by using both this MHD balance equation and the Ampere's law.

2.2.2 Cobb's pressure model for Grad-Shafranov equation

The equilibrium solution of a FRC is obtained from Eq.(2.29) and the Maxwell equations. These equations can be reduced to the Grad-Shafranov equation. First, let us explain how to derive the Grad-Shafranov equation. We can introduce the poloidal magnetic flux function Ψ which satisfies a following relation as $\boldsymbol{B}$,

$$\boldsymbol{B} \cdot \nabla \Psi = 0 \,. \tag{2.30}$$

A magnetic field must be divergence-free, i.e.,

$$\nabla \cdot \boldsymbol{B} = 0 \,. \tag{2.31}$$

We use a cylindrical coordinate system (r, ϕ, z) and assume the two-dimensional axisymmetric profile $(\partial/\partial\phi = 0)$. Then Eqs. (2.30) and (2.31) give rise to the following relations as

$$B_r = -\frac{1}{r}\frac{\partial \Psi}{\partial z} \,, \tag{2.32}$$

$$B_z = \frac{1}{r}\frac{\partial \Psi}{\partial r} \,, \tag{2.33}$$

$$B_\phi = 0 \,. \tag{2.34}$$

From the force balance equation (2.29), we have

$$\boldsymbol{B} \cdot \nabla P = 0 \,. \tag{2.35}$$

Solution of P satisfying Eq.(2.35) is given by an arbitrary function of Ψ, i.e.,

$$P = P(\Psi) \ . \tag{2.36}$$

It is assumed that there is no toroidal field ($B_\phi = 0$) and the diamagnetic current density $\boldsymbol{j}_d$ has only ϕ component, i.e., $\boldsymbol{j}_d = (0, j_\phi, 0)$. Then, the r component of Eq.(2.29) reduces to

$$\frac{dP(\Psi)}{d\Psi}\frac{\partial \Psi}{\partial r} = \frac{1}{c} j_\phi \frac{1}{r}\frac{\partial \Psi}{\partial r} \ , \tag{2.37}$$

or,

$$j_\phi = cr\frac{dP(\Psi)}{d\Psi} \ . \tag{2.38}$$

The Ampere's law $(4\pi/c)\boldsymbol{j}_d = \nabla \times \boldsymbol{B}$ becomes

$$\frac{4\pi}{c} j_\phi = -\frac{\partial}{\partial r}\left(\frac{1}{r}\frac{\partial \Psi}{\partial r}\right) - \frac{1}{r}\frac{\partial^2 \Psi}{\partial z^2} \ . \tag{2.39}$$

This equation is rewritten by using Eq.(2.38)

$$\triangle^* \Psi = -4\pi r^2 \frac{dP}{d\Psi} \ , \tag{2.40}$$

where $\triangle^*$ is the operator defined by

$$\triangle^* \equiv r\frac{\partial}{\partial r}\left(\frac{1}{r}\frac{\partial}{\partial r}\right) + \frac{\partial^2}{\partial z^2} \ . \tag{2.41}$$

Eq.(2.40) represents the Grad-Shafranov equation in axisymmetric cylindrical coordinate system.

We need to determine the functional form of $P(\Psi)$ to get the solution of this equation. Until now, various forms has been investigated to bring them close to realistic configuration. Here we adopt the Cobb's pressure model, which can control both the current profile and the beta value at the separatrix easily [46],

$$P(\Psi) = \begin{cases} P_0(K_0 - \chi - \frac{1}{2}D\chi^2) & \text{for } \chi \leq 0 \ ; \text{ inside separatrix} \\ P_0 K_0 e^{-\chi/K_0} & \text{for } \chi > 0 \ ; \text{ outside separatrix} \ , \end{cases} \tag{2.42}$$

where $\chi = \Psi/|\Psi_{ax}|$, Ψ_{ax} is the value of Ψ at the field null ($\chi = -1$), and P_0 is constant. K_0 is represented by two important parameters, β_{sp} and D as

$$K_0 = \beta_{sp}\left(\frac{1 - D/2}{1 - \beta_{sp}}\right). \tag{2.43}$$

The parameter β_{sp} is the normalized pressure value at the magnetic separatrix on the midplane and also represents roughly the plasma beta value at the separatrix,

$$\begin{aligned} \beta_{sp} &\equiv \frac{P(\chi = 0)}{P(\chi = -1)} \\ &= \frac{P(\chi = 0)}{B^2_{wall}/8\pi}\,. \end{aligned} \tag{2.44}$$

The last equality comes from the pressure balance in the radial direction on the midplane. D is the hollowness parameter which control the current distribution in the radial direction. That is to say, the current profile of the equilibrium state becomes peaked for $D < 0$, flat for $D = 0$, and hollow for $D > 0$ (see Fig.2.1). The hollowness parameter was first introduced by Steinhauer and Ishida [45], though their definition is a little different from that of D [see Eq.(1.15)]. We will solve the Grad-Shafranov equation with using this Cobb's pressure model later.

2.2.3 Modified equilibrium with beam ions

In the case where the beam ions exists, we cannot adopt the solution of the Grad-Shafranov equation directly. We must solve the following equations numerically instead.

$$-\nabla P + \frac{1}{c}\boldsymbol{j}_d \times \boldsymbol{B} = 0\,. \tag{2.45}$$

$$\nabla \times \boldsymbol{B} = \frac{4\pi}{c}(\boldsymbol{j}_d + \boldsymbol{j}_b)\,, \tag{2.46}$$

where $\boldsymbol{j}_b$ is the beam current density, the subscripts b denotes the beam component. In order to solve Eq.(2.45) and (2.46), we need the information of beam ions, i.e., their

positions x_b and velocities v_b. The force balance equation of a beam ion in the stationary state is given by

$$m_b(\boldsymbol{v}_b \cdot \nabla)\boldsymbol{v}_b = q_b \left(\boldsymbol{E}(\boldsymbol{x}_b) + \frac{\boldsymbol{v}_b}{c} \times \boldsymbol{B}(\boldsymbol{x}_b) \right) . \tag{2.47}$$

We assume that the only azimuthal component of beam velocity is not zero [$\boldsymbol{v}_b = (0, v, 0)$]. Then, the radial component of Eq.(2.47) is reduced to

$$- m_b \frac{v^2}{r} = q_b E_r + \frac{q_b}{c} v B_z . \tag{2.48}$$

From Eq.(2.23), the electric field is expressed by the ion pressure as

$$\begin{aligned} E_r &= \frac{1}{q_i n_i} \frac{\partial P_i}{\partial r} \\ &= \frac{1}{q_i} \frac{k_B T}{P_i} \frac{\partial P_i}{\partial r} \\ &= \frac{k_B T}{q_i} \frac{\partial}{\partial r} (\ln P_i) , \end{aligned} \tag{2.49}$$

where we assumed the equation of state for an ideal gas, i.e., $P_i = n_i k_B T$ ($T_i = T_e = T$, where subscript i and e denotes the quantities for ions and electrons, respectively, and temperature is spatially uniform). Substituting Eq.(2.49) into Eq.(2.48), we can obtain the following expression,

$$- m_i \frac{v^2}{r} = k_B T \frac{\partial}{\partial r} (\ln P_i) + \frac{q_i}{c} v B_z , \tag{2.50}$$

where we consider beam ions to be the same kind of background ions (i.e., $m_b = m_i$ and $q_b = q_i$). The current density of beam ions $\boldsymbol{j}_b$ is determined by the position and the velocity which satisfies Eq.(2.50). For an example, the current density of concentrated beam is expressed by the Delta function as,

$$j_b(r, z) = \frac{q_i N_b}{2\pi} \frac{v_b}{r_b} \delta(r - r_b) \delta(z) , \tag{2.51}$$

where r_b is the radial position, v_b is the azimuthal velocity, q_i is the ion charge, and N_b is the total number of beam ions. However, this expression is not practical in performing the numerical simulation because the current density becomes infinite at the beam position. In order to avoid this difficulty, we adopt the Gaussian distribution as,

$$j_b(r,z) \sim \exp\left[-\kappa^2\left\{\left(\frac{r-r_b}{r_1}\right)^2+\left(\frac{z}{z_1}\right)^2\right\}\right] , \tag{2.52}$$

where $r_1 = (r_{sp} - R)/2$, $z_1 = Er_1, (E = Z_{sp}/r_{sp})$, the dimensionless parameter κ determines the beam concentration. For simplicity, we fix the parameter κ to 2 in this thesis. The proportional constant in Eq.(2.52) is determined so as to satisfy the relation $I_b = \int j_b(r,z)drdz$ for a given value of I_b, where the integration is executed on the poloidal cross section.

A set of Eqs.(2.45), (2.46), and (2.50) determines the initial equilibrium profile of a FRC with beam ions. Let us consider how to solve these equations numerically. Eqs.(2.45), (2.46), and (2.50) reduce to

$$j_d = cr\frac{dP}{d\Psi} , \tag{2.53}$$

$$-\frac{c}{4\pi}\left(\frac{\partial}{\partial r}\frac{1}{r}\frac{\partial\Psi}{\partial r}+\frac{1}{r}\frac{\partial^2\Psi}{\partial z^2}\right) = j_d + j_b , \tag{2.54}$$

$$m_i\frac{v^2}{r} + k_B T\frac{\partial}{\partial r}(\ln P_i) + \frac{q_i}{c}vB_z = 0 . \tag{2.55}$$

First of all, we normalize the physical quantities, in Eq.(2.53),(2.54), the following quantities are introduced,

$$\begin{aligned} r &\rightarrow r_D\tilde{\tilde{r}} , \\ \Psi &\rightarrow r_D^2 B_N\tilde{\tilde{\Psi}} , \\ j &\rightarrow \frac{c}{4\pi}\frac{B_N}{r_D}\tilde{\tilde{j}} , \\ P &\rightarrow \frac{B_N^2}{4\pi}\tilde{\tilde{P}} , \end{aligned}$$

$$v \rightarrow v_{Ti}\tilde{\tilde{v}} ,$$

where the double tilde means the normalized quantity, r_D is the conducting wall radius, and B_N is the vacuum magnetic field. By using these fundamental physical quantities, we have

$$\tilde{\tilde{j}}_d = \tilde{\tilde{r}}\frac{\partial \tilde{\tilde{P}}}{\partial \tilde{\tilde{\Psi}}} , \tag{2.56}$$

$$-\frac{\partial}{\partial \tilde{\tilde{r}}}\frac{1}{\tilde{\tilde{r}}}\frac{\partial \tilde{\tilde{\Psi}}}{\partial \tilde{\tilde{r}}} - \frac{1}{\tilde{\tilde{r}}}\frac{\partial^2 \tilde{\tilde{\Psi}}}{\partial \tilde{\tilde{z}}^2} = \tilde{\tilde{j}}_d + \tilde{\tilde{j}}_b , \tag{2.57}$$

$$\frac{\tilde{\tilde{v}}^2}{\tilde{\tilde{r}}} + \frac{\partial}{\partial \tilde{\tilde{r}}}(\ln \tilde{\tilde{P}}_i) + \frac{1}{\tilde{\tilde{\lambda}}_i}(\tilde{\tilde{v}}\tilde{\tilde{B}}_z) = 0 , \tag{2.58}$$

where $\lambda_i = v_{Ti}/\omega_{ci}$, $\omega_{ci} = q_i B_N/m_i c$. By solving Eqs.(2.56),(2.57), and (2.58) self-consistently we get the initial profile [$P(r,z)$, $\boldsymbol{B}(r,z)$, $\boldsymbol{j}_d(r,z)$, and $\boldsymbol{j}_b(r,z)$] for particle simulation.

2.2.4 Numerical solutions

Let us solve a set of Eqs.(2.56),(2.57) and (2.58) with an iteration method. The main procedure of the numerical calculation is as follows [66]. First, we put the trial form of the current density into the r.h.s. of Eq.(2.57). Then, Eq.(2.57) is solved numerically in terms of $\Psi(r,z)$. Then, we get the solution of the first iteration $\Psi^{(1)}$. Second, since the functional form of pressure is given by Cobb's model, the diamagnetic current $\boldsymbol{j}_d^{(1)}(r,z)$ can be determined by substituting the obtained solution $\Psi^{(1)}$ into Eq.(2.56). The stable orbit of a beam ion in the given field $\boldsymbol{B}^{(1)}$ can be calculated from Eq.(2.58), which determines the beam current $\boldsymbol{j}_b^{(1)}$. Thus we can obtain the total current density as

$$\boldsymbol{j}_{tot}^{(1)}(r,z) = \boldsymbol{j}_d^{(1)}(r,z) + \boldsymbol{j}_b^{(1)}(r,z) . \tag{2.59}$$

Substitute Eq.(2.59) into Eq.(2.57) and solve it again, then we get the solution of the second iteration $\Psi^{(2)}$. We must repeat this process until the solution satisfies the convergence condition $|\Psi^{(n)} - \Psi^{(n-1)}| < \epsilon$ (ϵ : small number).

Let us now show the several examples of the equilibrium solution obtained by this method. The equilibrium profile are altered markedly as the profile control parameters, β_{sp} and D, are changed. By examining the parameter dependence of the equilibrium solution we find three important features in it. Figure 2.2 shows the contour plots of the pressure in the poloidal cross section for the six cases with different values of D and β_{sp} where the top line indicates the vessel wall, the bottom line indicates the symmetrical axis, and the right line corresponds to the midplane on each figure. The dependence of the profile on β_{sp} for peaked current profile ($D = -0.6$) are shown in the left three panels. The first feature is that the spatial distribution tends to spread over the outer region of the separatrix as β_{sp} increases. The second important feature is the shape of the separatrix. The contours of the poloidal flux function are shown in Fig. 2.3 for the same cases as Fig. 2.2. The shape is the racetrackness for small β_{sp} case ($\beta_{sp} = 0.02$) and elliptical for large β_{sp} case ($\beta_{sp} = 0.20$). The third important point is that the radial distribution of J_ϕ/r changes according to the value of the hollowness parameter D, as is shown in Fig.2.4. We use these solutions as the initial conditions of the particle simulation.

Finally, it is necessary, at this point, to explain the representation of the kinetic parameters $\bar{s}$ in connection with the MHD equilibrium configuration. We may recall that the parameter $\bar{s}$ is defined by Eq.(1.14)

$$\bar{s} = \int_R^{r_{sp}} \frac{r dr}{r_{sp} \lambda_i} . \tag{2.60}$$

In this expression, the local ion Larmor radius λ_i is given by

$$\begin{aligned}
\lambda_i &= \sqrt{\frac{k_B T_i}{m_i}} \frac{m_i c}{q_i B_z(r)} \\
&= \sqrt{\frac{k_B T_i}{m_i}} \frac{m_i c}{q_i B_N} \frac{1}{\tilde{\tilde{B}}_z(r)} \\
&= v_{T_i} \omega_{ci}^{-1} \frac{1}{\tilde{\tilde{B}}_z(r)} \\
&= \lambda_0 / \tilde{\tilde{B}}_z(r) \,, \qquad (2.61)
\end{aligned}$$

where λ_0 is the ion Larmor radius defined by the external magnetic field B_N, and $B_z(r)$ is the magnetic field component at the midplane. By using these quantities, the parameter $\bar{s}$ is reduced to

$$\begin{aligned}
\bar{s} &= \int_R^{r_{sp}} \frac{r \tilde{\tilde{B}}_z dr}{r_{sp} \lambda_0} \\
&= \frac{1}{\tilde{\tilde{r}}_{sp} \tilde{\tilde{\lambda}}_0} \int_{\tilde{\tilde{R}}}^{\tilde{\tilde{r}}_{sp}} \tilde{\tilde{r}} \tilde{\tilde{B}}_z d\tilde{\tilde{r}} \\
&= \frac{1}{\tilde{\tilde{r}}_{sp} \tilde{\tilde{\lambda}}_0} \left[\tilde{\tilde{\Psi}}(\tilde{\tilde{r}}_{sp}) - \tilde{\tilde{\Psi}}(\tilde{\tilde{R}}) \right] \\
&= -\tilde{\tilde{\Psi}}(\tilde{\tilde{R}}) / \tilde{\tilde{r}}_{sp} \tilde{\tilde{\lambda}}_0 \,, \qquad (2.62)
\end{aligned}$$

where the relations $\Psi(r_{sp}) = 0$ and $T = constant$ are used. Equation (2.62) is rewritten as

$$\tilde{\tilde{\lambda}}_0 = -\frac{\tilde{\tilde{\Psi}}(\tilde{\tilde{R}})}{\bar{s}\ \tilde{\tilde{r}}_{sp}}. \qquad (2.63)$$

When the MHD equilibrium configuration is solved and the $\bar{s}$-value is designated, Eq.(2.63) determines the particle temperature which is needed for the particle initial distribution.

2.3 Boundary condition

We consider the FRC plasma confined by a uniform external magnetic field within the cylindrical conducting vessel. Thus, the suitable boundary condition should be imposed to both the field quantities, electric field $\boldsymbol{E}$ and the magnetic field $\boldsymbol{B}$, and the particle quantities, position $\boldsymbol{x}_j$ and velocity $\boldsymbol{v}_j$. The boundary conditions for these quantities are explained in this section.

2.3.1 Field quantities

It is assumed that the physical quantities are periodic at the boundary of z axis and the vessel wall is a rigid perfect conductor. Therefore, the field quantities should satisfy the following conditions at the cylindrical wall ($r = r_D$),

$$\boldsymbol{n} \cdot \boldsymbol{B}\,|_{r=r_D} = 0\,, \tag{2.64}$$

$$\boldsymbol{n} \times \boldsymbol{E}\,|_{r=r_D} = 0\,, \tag{2.65}$$

where $\boldsymbol{n}$ denotes the unit vector pointing inward along r. The tangential component of the magnetic field and the perpendicular component of the electric field at the conducting wall are given by solving the Maxwell equations.

2.3.2 Particle quantities

It is assumed that the particles are elastically reflected at the vessel wall and are imposed the periodic boundary condition in the axial direction. That is, if a particle comes outside the conducting wall, its radial position r_j and radial velocity v_{jr} are replaced by the following rules,

$$v_{jr} \;\Rightarrow\; -v_{jr}\;, \tag{2.66}$$

$$r_j \;\Rightarrow\; r_D - (r_j - r_D)\;. \tag{2.67}$$

2.4 Numerical scheme

We consider a FRC plasma which consists of ions and electrons which are treated as superparticles. To get the time evolution of a FRC plasma, the equations of motion of all particles and the Maxwell equations should be solved simultaneously. The outline of the numerical scheme is explained in this section.

2.4.1 Numerical modeling

The total number of thermal particles is fixed to 10^6. The number of beam ions can be changed freely in this simulation. The FRC plasma is confined by a uniform external magnetic field within the cylindrical conducting vessel. The height of this vessel Z_d is always fixed to 3 times the vessel radius r_D in this thesis. The ratio of ion to electron mass $m_i/m_e(= 50)$ and the frequency ratio $\omega_{pe}/\omega_{ce}(= 5.0)$ are kept unchanged for all cases, where $\omega_{ce}(= q_e B_{wall}/m_e c)$ is the electron cyclotron frequency defined by the magnetic field of the vessel wall on the midplane B_{wall}. Particle pusher and gather processes are carried out in the rectangular coordinates (x, y, z) where the simulation domain is implemented on a $(49 \times 49 \times 32)$ point grid and its volume is given by $(2r_D \times 2r_D \times 2Z_d)$. On the other hand, the electromagnetic field is solved in the cylindrical coordinates (r, ϕ, z) so that the boundary condition on the conducting wall can be satisfied with a high precision. The cylindrical vessel is embedded inside the rectangular simulation box so as to contact its surface with four sides of the rectangular box. The $(33 \times 32 \times 32)$ space grids are used in this calculation.

2.4.2 Superparticle

Here let us describe a numerical model of superparticles used for the present particle simulation. We adopt the second order model as a shape function of superparticles [68]. The shape function plays a role to transfer the particle informations given at the particle position (x_i) to the fluid quantities such as the current density and the charge density which are defined at the space grids. The form of a superparticle is expressed by a triangle with the base length equal to 2.0 times the grid separation ΔX (Fig.2.5) [68]. When we consider a particle at $x = x_i$, the position of the nearest space grid is represented by X_j and two neighboring space grids are $X_{j\pm1}$. The term "quadratic spline" can be defined as the way to assign the charge of a particle to the three grid points X_{j-1}, X_j, and X_{j+1} (Fig.2.6).

We define each charge at the grid points by assigning the charge of superparticles corresponding to the area of each superparticle occupied by each grid area. Therefore the charge q_{j-1} at the grid point X_{j-1} assigned by one superparticle with charge q_c is

$$\begin{aligned} q_{j-1} &= q_c \times \frac{1}{2}\frac{a}{\Delta X}\left[\frac{\Delta X}{2} - (x_i - X_j)\right]^2 / a\Delta X \\ &= \frac{q_c}{2}\left[\frac{1}{2} - \frac{x_i - X_j}{\Delta X}\right]^2, \end{aligned} \tag{2.68}$$

where a is the height of superparticle. The charge q_j and q_{j+1} at the grid point X_j and X_{j+1}, respectively are obtained in a similar way,

$$q_j = q_c\left[\frac{3}{4} - \left(\frac{x_i - X_j}{\Delta X}\right)^2\right], \tag{2.69}$$

$$q_{j+1} = \frac{q_c}{2}\left[\frac{1}{2} + \frac{x_i - X_j}{\Delta X}\right]^2. \tag{2.70}$$

From these expressions, one obtains the concrete form of S,

$$S(X_{j-1} - x_i) = \frac{1}{2\Delta X}\left[\frac{1}{2} - \frac{x_i - X_j}{\Delta X}\right]^2, \tag{2.71}$$

$$S(X_{j+1} - x_i) = \frac{1}{2\Delta X}\left[\frac{1}{2} + \frac{x_i - X_j}{\Delta X}\right]^2, \tag{2.72}$$

$$S(X_j - x_i) = \frac{1}{\Delta X}\left[\frac{3}{4} - \left(\frac{x_i - X_j}{\Delta X}\right)^2\right]. \tag{2.73}$$

In the three-dimensional case, this factor is composed of the factor of each dimension,

$$S(\boldsymbol{x}) = S(x)S(y)S(z)\ . \tag{2.74}$$

2.4.3 Time integration

We adopt the predictor-corrector method with a sub-stepping of the EM field for a time advancing. Namely, the particles are advanced with a large time step of $\omega_{pe}\Delta t = 1.5$ [69] while the EM field is advanced with a small time step of $(c\Delta t)/(\Delta\phi\Delta r) < 1.0$ ($\Delta\phi\Delta r$: minimum grid separation) [70] by using an iteration method.

Let us look briefly at the concrete technique for solving the basic equations. The equations of motion are solved explicitly for time advance,

$$\frac{d\boldsymbol{v}_j^n}{dt} = \frac{q_j}{m_j}\left[\boldsymbol{E}(\boldsymbol{x}_j^n) + \frac{\boldsymbol{v}_j^n}{c} \times \boldsymbol{B}(\boldsymbol{x}_j^n)\right], \tag{2.75}$$

$$\frac{d\boldsymbol{x}_j^{n+\frac{1}{2}}}{dt} = \boldsymbol{v}_j^{n+\frac{1}{2}}, \tag{2.76}$$

where superscripts and subscripts denote the time level and the physical quantities of j-th particle, respectively, i.e., q_j is a charge and m_j is a mass of j-th particle. The time derivatives are expressed by

$$\frac{d\boldsymbol{v}_j^n}{dt} = \frac{\boldsymbol{v}_j^{n+\frac{1}{2}} - \boldsymbol{v}_j^{n-\frac{1}{2}}}{\Delta t}, \tag{2.77}$$

$$\frac{d\boldsymbol{x}_j^{n+\frac{1}{2}}}{dt} = \frac{\boldsymbol{x}_j^{n+1} - \boldsymbol{x}_j^n}{\Delta t}. \tag{2.78}$$

On the other hand, Maxwell equations are solved implicitly,

$$\frac{1}{c}\frac{\partial \boldsymbol{B}^{n+\frac{1}{2}}}{\partial t} = -\nabla \times \boldsymbol{E}^{n+\alpha}, \tag{2.79}$$

$$\frac{1}{c}\frac{\partial \boldsymbol{E}^{n+\frac{1}{2}}}{\partial t} = \nabla \times \boldsymbol{B}^{n+\alpha} - \frac{4\pi}{c}\boldsymbol{j}^{n+\gamma}, \tag{2.80}$$

where the time derivatives are replaced by finite difference as

$$\frac{\partial \boldsymbol{B}^{n+\frac{1}{2}}}{\partial t} = \frac{\boldsymbol{B}^{n+1} - \boldsymbol{B}^{n}}{\Delta t}, \tag{2.81}$$

$$\frac{\partial \boldsymbol{E}^{n+\frac{1}{2}}}{\partial t} = \frac{\boldsymbol{E}^{n+1} - \boldsymbol{E}^{n}}{\Delta t}, \tag{2.82}$$

and time decentering parameter α and γ are used (we adopt $\alpha = \gamma = 0.6$ in this thesis). The physical quantities defined at the decentering time are obtained by a linear interpolation such as

$$\boldsymbol{E}^{n+\alpha} = \alpha \boldsymbol{E}^{n+1} + (1-\alpha)\boldsymbol{E}^{n}, \tag{2.83}$$

$$\boldsymbol{j}^{n+\gamma} = \left(\frac{3}{2} - \gamma\right)\boldsymbol{j}^{n+\frac{1}{2}} + \left(\gamma - \frac{1}{2}\right)\boldsymbol{j}^{n+\frac{3}{2}}. \tag{2.84}$$

Because the field quantities $\boldsymbol{E}^{n+1}$, $\boldsymbol{B}^{n+1}$, and $\boldsymbol{j}^{n+\frac{1}{2}}$ at the future time levels appear in the right hand sides of Eqs.(2.79) and (2.80), we cannot solve them explicitly. We will discuss the predictor and corrector technique employed to solve them in the followings.

(i) Predictor process

We assume that parameters α and γ equal 0.5, hence the current density $\boldsymbol{j}^{n+\frac{3}{2}}$ disappear in Maxwell equation. In the first place, we know the quantities $\boldsymbol{x}_j^n$, $\boldsymbol{v}_j^{n+\frac{1}{2}}$, $\boldsymbol{E}^n$, and $\boldsymbol{B}^n$. Solving Eq.(2.76), then we obtain $\boldsymbol{x}_j^{n+1}$. The current density $\boldsymbol{j}^{n+\frac{1}{2}}$ is obtained by using $\boldsymbol{x}_j^{n+\frac{1}{2}}$ $[= \frac{1}{2}(\boldsymbol{x}_j^n + \boldsymbol{x}_j^{n+1})]$ and $\boldsymbol{v}_j^{n+\frac{1}{2}}$. Then, Maxwell equations are reduced to

$$\frac{1}{c}\frac{1}{\Delta t}(\boldsymbol{B}^{n+1} - \boldsymbol{B}^{n}) = -\nabla \times \left(\frac{1}{2}\boldsymbol{E}^{n+1} + \frac{1}{2}\boldsymbol{E}^{n}\right), \tag{2.85}$$

$$\frac{1}{c}\frac{1}{\Delta t}(\boldsymbol{E}^{n+1} - \boldsymbol{E}^{n}) = \nabla \times \left(\frac{1}{2}\boldsymbol{B}^{n+1} + \frac{1}{2}\boldsymbol{B}^{n}\right) - \frac{4\pi}{c}\boldsymbol{j}^{n+\frac{1}{2}}. \tag{2.86}$$

We can solve these equations by iteration method and obtain the field quantities $\boldsymbol{E}^{n-1}$ and $\boldsymbol{B}^{n+1}$. Substitute $\boldsymbol{E}^{n+1}$, $\boldsymbol{B}^{n+1}$, and $\boldsymbol{v}^{n+\frac{1}{2}}$ into Eqs.(2.75) and (2.76), then, we can

obtain $\boldsymbol{v}_j^{n+\frac{3}{2}}$ and $\boldsymbol{x}_j^{n+\frac{3}{2}}$ which determines $\boldsymbol{j}^{n+\frac{3}{2}}$.

(ii) Corrector process

At the next step, we choose $\alpha = \gamma = 0.6$ and use the quantities $\boldsymbol{E}^n$, $\boldsymbol{B}^n$, $\boldsymbol{j}^{n+\frac{1}{2}}$, and $\boldsymbol{j}^{n-\frac{3}{2}}$ obtained in the predictor process. We solve Maxwell equations again and obtain $\boldsymbol{E}^{n+1}$ and $\boldsymbol{B}^{n+1}$. By using these quantities, we can get the particle position $\boldsymbol{x}_j^{n+1}$ and velocity $\boldsymbol{v}_j^{n+\frac{3}{2}}$.

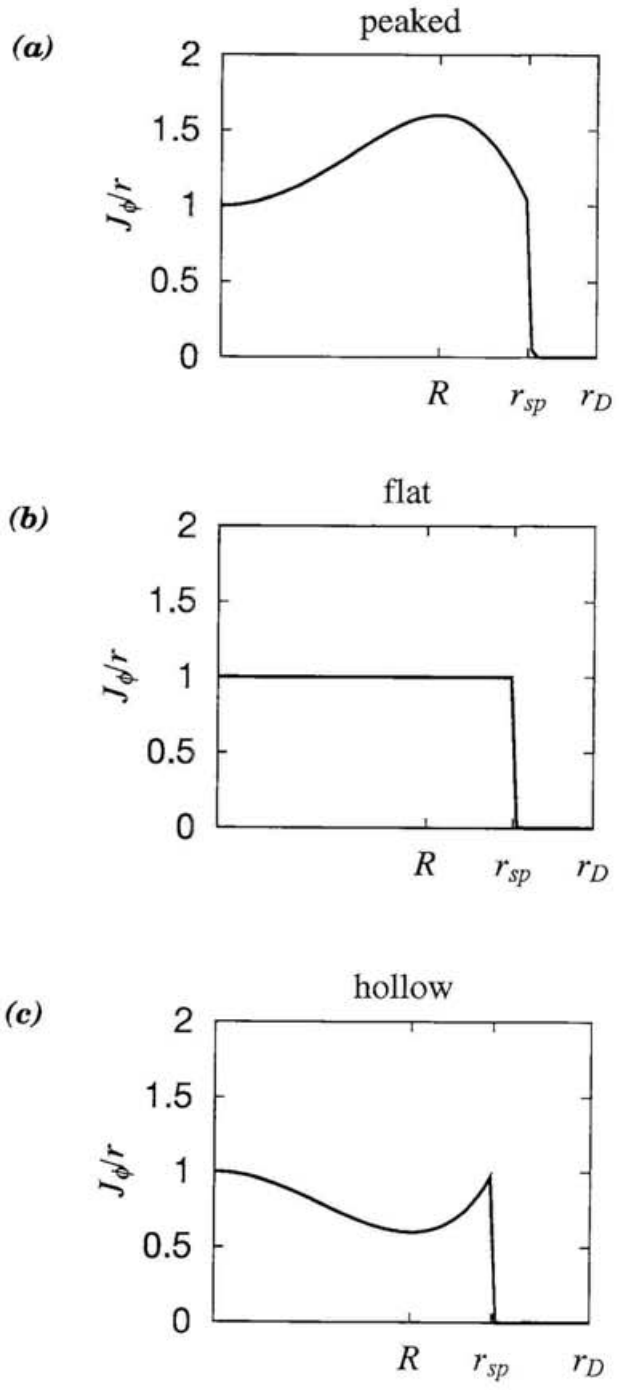

Figure 2.1: Radial profile of toroidal current density for the case when $\beta_{sp} = 0.02$ and (a) $D = -0.6$ (peaked profile), (b) $D = 0.0$ (flat profile), (c) $D = 0.4$ (hollow profile).

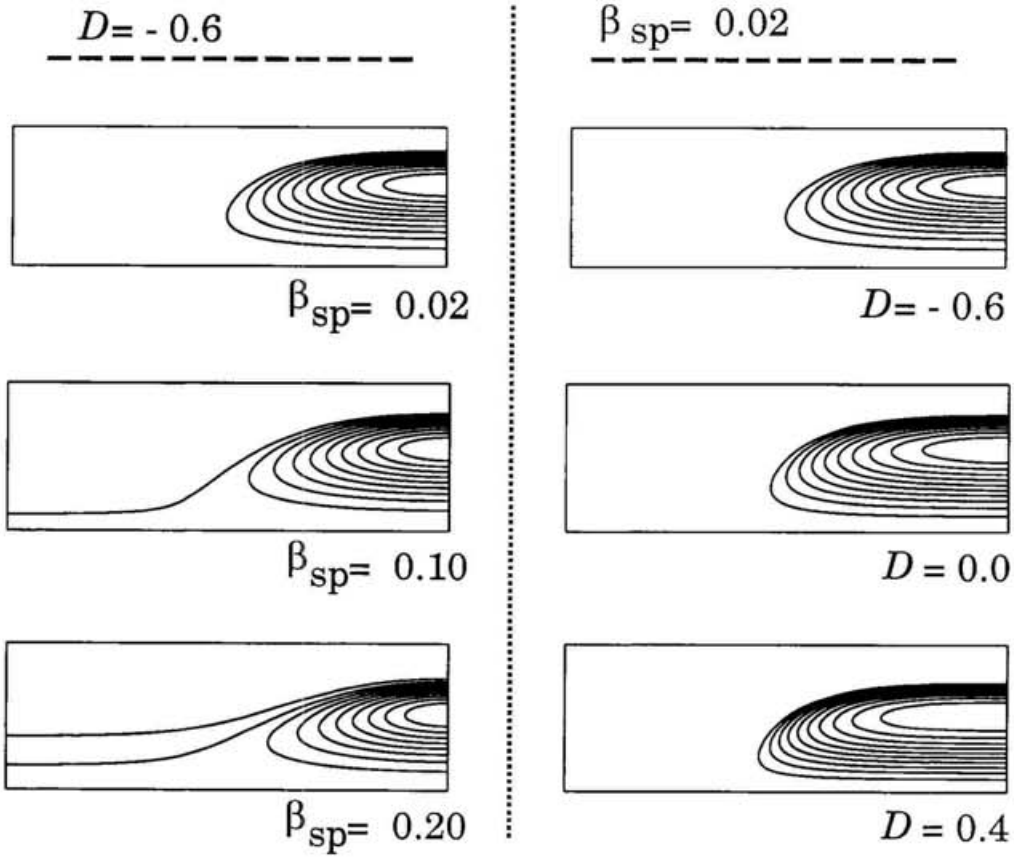

Figure 2.2: Contour plots of pressure profile in the poloidal plane.

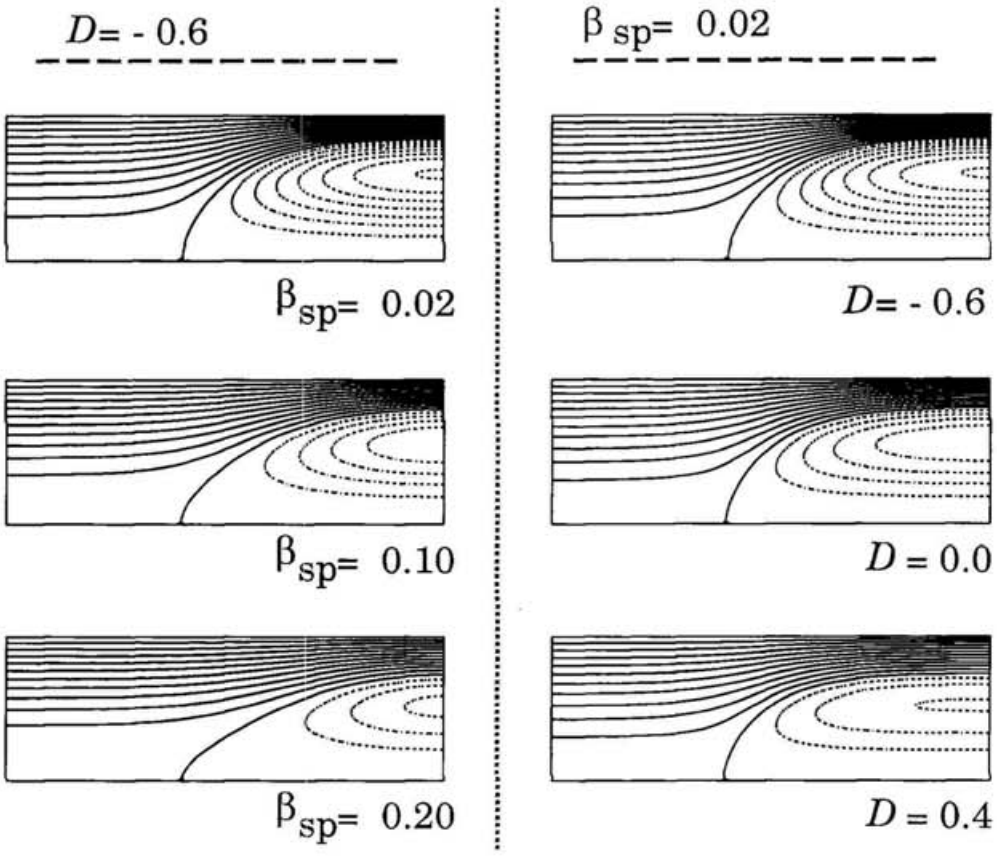

Figure 2.3: Contour plots of poloidal flux in the poloidal plane.

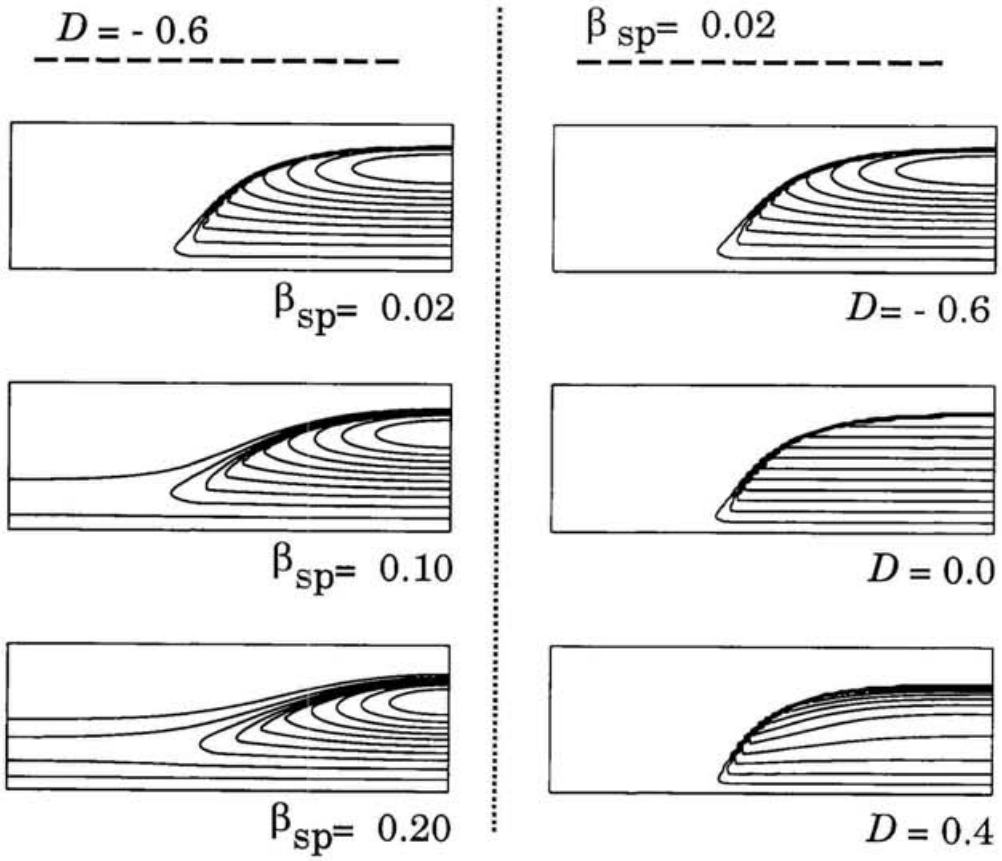

Figure 2.4: Contour plots of toroidal current density in the poloidal plane.

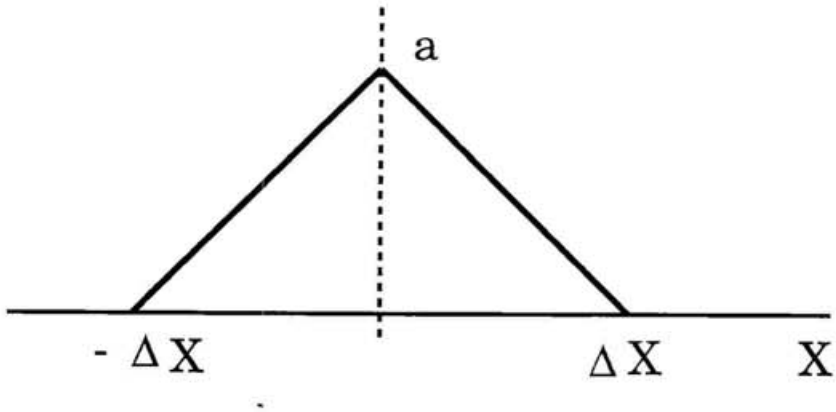

Figure 2.5: Shape of a superparticle for one dimension :ΔX and a mean the grid separation and the height of superparticle, respectively.

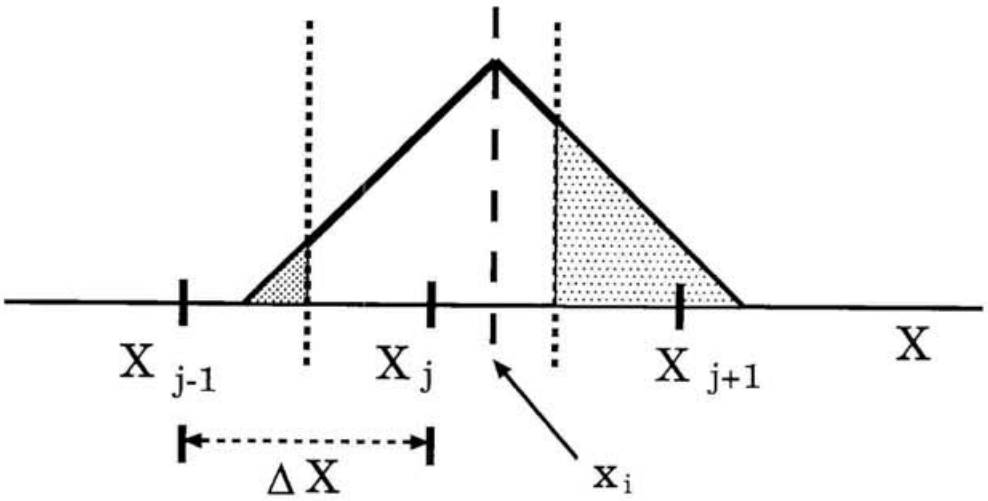

Figure 2.6: Assignment of a superparticle to grid points: x_i denotes the position of a superparticle, X_j is the nearest-neighboring grid point

Chapter 3

Simulation results

3.1 Stabilization by cycling ions crossing magnetic separatrix

In this section, we shall focus on both the finite ion Larmor radius effect and the profile control effect [71]. That is to say, the parameters which control the ion beam effect, the number ratio of beam ions to thermal ions N_b/N_i and the current ratio of beam ions to background plasma I_b/I_p, are always taken to zero. The parameters used for the simulation are listed in Table 3.1. In the present model, three parameters can be controlled independently. The first is the parameter $\bar{s}$ which controls the finite ion Larmor radius effect. The others are the profile control parameters β_{sp} and D which determine the pressure at the separatrix, and the hollowness of the current profile, respectively.

3.1.1 Simulation result

We carry out several simulation runs for a moderately kinetic plasma of $2 \leq \bar{s} \leq 5$, because the discrepancy between the theories and the experiments becomes most distinct in this region. Let us examine the behaviors of the tilt instability based on the simulation results for the typical case R1. Figures 3.1 and 3.2 display the spatial profiles of vector plots of mass flux density (Fig. 3.1) and those of contour plots of mass density (Fig. 3.2) in the poloidal cross section at four different time periods, where the mass flux density $\boldsymbol{f}_m(\boldsymbol{x}, t)$ and the mass density $\rho_m(\boldsymbol{x}, t)$ are defined as

$$\boldsymbol{f}_m(\boldsymbol{x}, t) = \sum_{j=1}^{N} m_j \boldsymbol{v}_j(t)\ S[\boldsymbol{x} - \boldsymbol{x}_j(t)]\,, \tag{3.1}$$

$$\rho_m(\boldsymbol{x}, t) = \sum_{j=1}^{N} m_j\ S[\boldsymbol{x} - \boldsymbol{x}_j(t)]\,, \tag{3.2}$$

and time is normalized by the Alfvén transit time $t_A (= r_D/V_A : V_A$ is Alfvén velocity estimated from the magnetic field B_{wall} and the ion density at the field-null). It is clearly seen in Fig. 3.1 that the asymmetric flow with respect to the z axis grows gradually as time goes on. As a result of the development of the tilt motion, two peaks of density contours move in the opposite directions to each other. The development of tilt instability is hereafter expressed in terms of the Fourier amplitude of the z-component of the fluid velocity $V_z^{(1)}(t)$, where superscript (1) denotes the azimuthal mode number $n = 1$, and the other spatial dependences are eliminated by averaging it over the (r, z) space.

Three kinds of simulation runs are carried out to investigate the dependence of the tilt instability on the parameters $\bar{s}$, β_{sp}, and D. The dependence of the tilt mode $V_z^{(1)}(t)$ on β_{sp} are shown in Figure 3.3 where $\bar{s} = 3.0$, $D = -0.6$, and β_{sp} is equal to 0.02 (R1), 0.10 (R2), and 0.20 (R3), respectively. The growth rate of the tilt mode normalized by

MHD one, γ/γ_M, is listed in Table 3.1 where MHD growth rate γ_M [33,35] is defined by

$$\gamma_M = C\frac{\tilde{V}_A}{Z_{sp}}, \tag{3.3}$$

$\tilde{V}_A$ is the average Alfvén velocity associated with the volume-averaged magnetic field and the ion density at the field-null, and Z_{sp} is the separatrix half-length along the z axis. The coefficient C in Eq. (3.3), which is of the order of unity and depends on the configuration of magnetic separatrix, is fixed to 3 in this thesis [35]. Figure 3.3 clearly shows that the growth rate γ/γ_M decreases dramatically with increasing β_{sp} and thus the tilt mode can be stabilized for a high $\beta_{sp}(= 0.2)$.

The finite ion Larmor radius effect on the tilt mode is examined for a low $\beta_{sp}(= 0.02)$ plasma with a peaked current profile ($D = -0.6$), when $\bar{s}$ varies in a moderately kinetic regime of $2 \leq \bar{s} \leq 5$. The growth rates of tilt mode are listed in the cases R1($\bar{s} = 3$), R4($\bar{s} = 2$), and R5($\bar{s} = 5$) of Table 3.1. We cannot find any distinct differences among the growth rates. On the contrary, the previous particle simulation [44] indicated that the growth rate of tilt mode decreases with decreasing $\bar{s}$. The difference between the previous and our results may be explained by following reasons. The previous simulation [44] adopted the rigid rotor model in which average ion velocity along the azimuthal direction increases as the radial location moves outwards and $\bar{s}$ decreases. Thus, the stabilization by the ions with a high rotational velocity may be more efficient with decreasing $\bar{s}$.

The dependence of the tilt mode on the hollowness parameters is examined for a low $\beta_{sp}(= 0.02)$ and moderately kinetic ($\bar{s} = 3$) plasma, where D is equal to -0.6 (R1), 0.0 (R8), and 0.4 (R6), respectively. It is found that the tilt mode, the growth rate of which is listed in Table 3.1, are hardly affected by the hollowness parameter for low β_{sp} and moderately kinetic plasmas. Cobb *et al.* [46] showed by using an extended MHD model with Hall terms that the tilt mode tends to be stable if β_{sp} is enough high and the current

profile is hollow. In their model, however, $\bar{s}$ decreases as the current profile becomes hollow and the stable configuration is realized in kinetic plasmas of $\bar{s} \approx 1$. Therefore, we cannot identify from their results whether this stabilization comes from the profile control effect or the finite ion Larmor radius effect.

These results lead us to the conclusion that both the finite ion Larmor radius effect (parameter $\bar{s}$) and the profile control effect (hollowness parameter D) are not efficient for low β_{sp} and moderately kinetic plasmas, but the tilt stabilization effect becomes significant for high β_{sp} plasmas ($\beta_{sp} \geq 0.2$), even if plasmas are moderately kinetic ($\bar{s} = 3.0$) and the current profile is peaked ($D = -6.0$).

3.1.2 Stabilization mechanism by cycling ions

In order to clarify the stabilization mechanism when the parameter β_{sp} increases, we focus on the role of the ions which move across the separatrix repeatedly (we call them "cycling ions" to distinguish them from the other ions). Whether an ion is cycling or non-cycling is determined by tracing its orbit in a real space. The motion of ions in a FRC is complex, because magnetic field varies spatially and its scale is comparable to the orbit amplitude. Two typical examples of ion orbits in the (r, ϕ) plane are demonstrated in Figure 3.4 for the case R3, where the solid and broken circles stand for the conducting wall and the magnetic separatrix in the midplane, respectively. The ions with a relatively small energy move along the gradient-$\boldsymbol{B}$ drift orbit [Fig. 3.4(a)], while the ions with a larger energy than a critical value [44] execute a complex motion crossing the field-null line, which is called "a meandering motion" [Fig. 3.4(b)]. The ion orbits are roughly classified into these two motions regardless of whether they are cycling or non-cycling. The percentage of cycling ions executing gradient-$\boldsymbol{B}$ drifting motion increases as β_{sp} increases. For example,

the percentage is about 1.2% for the case R1 ($\beta_{sp} = 0.02$), and about 3.5% for the case R3 ($\beta_{sp} = 0.20$). One can find in Fig. 3.4 that a cycling, meandering ion spends most of its time inside the separatrix, while a cycling, gyrating ion exists outside the separatrix as long as inside the separatrix.

Let us define the number flux of cycling ions by the total number which times cycling ions move across the magnetic separatrix in one Alfvén time. For example, if an ion move across the separatrix three times in one Alfvén time, the number flux of this ion is counted three. The average number flux of cycling ions is shown as a function of β_{sp} in Fig. 3.5 for all cases, where the number flux divided by the total number of ions is displayed. The number flux increases monotonously as β_{sp} increases. In contrast to this, the number flux weakly depends on the values of $\bar{s}$ and D (see three points at $\beta_{sp} = 0.1$ and six points at $\beta_{sp} = 0.02$ in Fig. 3.5). That is, the changes in the flux when $\bar{s}$ decreases or the current profile becomes hollow are much smaller compared with that when β_{sp} increases. Figure 3.6 shows the growth rate as a function of the average number flux of cycling ions for all cases from R1 to R10 in Table 3.1. It is important to note that there is a clear correlation between the average number flux and the growth rate of tilt mode, i.e., the larger the average flux is, the smaller the growth rate becomes. In other words, cycling ions crossing the magnetic separatrix contribute to the stabilization of the tilt mode.

Before examining the role of the cycling ions, a few remarks should be made concerning the driving force of tilt instability. There are three force terms to create the plasma motion along the z axis in the fluid equation, i.e., $\rho \boldsymbol{E}_z$, $(\boldsymbol{j} \times \boldsymbol{B})_z$, and $\partial P/\partial z$. Figure 3.7 indicates the time histories of $n = 1$ mode of force terms for the case R1. While the amplitude of $(\partial P/\partial z)^{(1)}$ (dot-dashed line) and $(\rho \boldsymbol{E}_z)^{(1)}$ (dotted line) remain at the initial fluctuation level, the amplitude of $(\boldsymbol{j} \times \boldsymbol{B})_z^{(1)}$ increases gradually as time elapses. It is clear from these

results that the $(\boldsymbol{j} \times \boldsymbol{B})_z$ force is the dominant component to lead to the tilt instability. Accordingly, we will focus on the behavior of the $(\boldsymbol{j} \times \boldsymbol{B})_z$ force later.

In order to elucidate the physical picture of the tilt stabilization by the cycling ions, let us expand the current density into the cycling component $\boldsymbol{j}^{(c)}$ and the non-cycling component $\boldsymbol{j}^{(n)}$. The force $(\boldsymbol{j} \times \boldsymbol{B})_z^{(1)}$ which generates the tilt motion along the z direction in the plasma can be calculated with these two components separately. Suppose that the Fourier expansion in terms of the toroidal angle ϕ takes the following form as

$$[\boldsymbol{j}^{(\alpha)} \times \boldsymbol{B}]_z^{(1)} = A^{(\alpha)}(r,z)\cos\phi + B^{(\alpha)}(r,z)\sin\phi\,, \tag{3.4}$$

where the superscript (α) denotes a cycling component $(\alpha = c)$ or a non-cycling component $(\alpha = n)$. We can define the average amplitude of the force $F^{(\alpha)}(t)$ and the phase difference $\delta\phi$ between the forces acting on the cycling ions and the non-cycling ions as

$$F^{(\alpha)}(t) = \sqrt{\langle A^{(\alpha)}\rangle^2 + \langle B^{(\alpha)}\rangle^2}\,, \tag{3.5}$$

$$\delta\phi = \tan^{-1}\frac{\langle B^{(n)}\rangle}{\langle A^{(n)}\rangle} - \tan^{-1}\frac{\langle B^{(c)}\rangle}{\langle A^{(c)}\rangle}\,, \tag{3.6}$$

where $\langle\rangle$ stands for the average over the (r,z) space, i.e., $\langle A(r,z)\rangle = \int A(r,z)drdz$. Figure 3.8 shows the time evolutions of (a) the amplitudes and (b) the phase difference for the unstable case R4 where the solid and dotted lines in Fig. 3.8(a) represent the forces acting on the cycling ions and the non-cycling ions, respectively. The phase difference is nearly equal to $-\pi$ at $t = 0$, i.e., the directions of two forces are opposite to each other. The difference, however, tends to decrease as time elapses and remains nearly equal to zero for $t > 1.8t_A$. Thus, one component of the $\boldsymbol{j} \times \boldsymbol{B}$ force works synchronously on the plasma to the same direction as the other component so that the tilt instability grows swiftly on the whole. Figure 3.9 shows the time evolutions of (a) the amplitudes of the tilt forces and (b) their phase difference for the stable case R3. It is important to note in Fig. 3.9 that

the amplitudes remain much smaller than those for the unstable case R4 [Fig. 3.9(a)], and the phase difference is always large ($\delta\phi \sim \pm\pi$) [Fig. 3.9(b)]. If we take into account the fact that two forces have always the same amplitude [see Fig. 3.9(a)], it is concluded that the $\boldsymbol{j} \times \boldsymbol{B}$ force by the cycling ions works on the plasma so as to cancel the tilting force by the non-cycling ions and thus the tilt mode can be stabilized for a large number flux of cycling ions.

3.1.3 Summary and discussions

The stabilization of the tilt disruption in a FRC plasma by both the finite ion Larmor radius effect and the profile control effect is investigated by means of a three-dimensional particle simulation. By carrying out the simulation runs with different values of β_{sp}, $\bar{s}$, and D for a moderately kinetic plasma ($2 \leq \bar{s} \leq 5$), we have clarified that it is effective against the tilt instability to increase the separatrix beta value (β_{sp}) and the tilt mode can be stabilized for a high β_{sp} (≥ 0.2). On the other hand, the stabilization of tilt mode can be scarcely altered by changing the $\bar{s}$ value and the current profile for low β_{sp} (≤ 0.1) and moderately kinetic plasmas. The detailed analysis reveals that the number flux of the ions crossing the magnetic separatrix repeatedly ("cycling ions") increases in proportion to β_{sp} and the tilt stability is realized for a large number flux of cycling ions.

The stabilization mechanism by cycling ions is as follows. Tilt instability is triggered by the internal mode, i.e., the collective motion of plasma is generated inside the magnetic separatrix. The ions which make a cyclic motion across the separatrix are not able to follow the collective motion when they move outside the separatrix. The phase difference between cycling ions and non-cycling ions is created in proportion to the period during which cycling ions exist outside the separatrix. When cycling ions come back inside the

separatrix, the internal tilting motion is disturbed by the motion of cycling ions. The orbits of cycling ions are roughly classified into a gradient-$\boldsymbol{B}$ drift orbit and a meandering orbit, as was shown in Fig. 3.4 . The cycling ions executing a gradient-$\boldsymbol{B}$ drift exist outside the separatrix as long as inside the separatrix. Therefore, they play a role to suppress the tilting motion because their motion is out of phase with the tilting motion. The number of cycling, gyrating ions increase as β_{sp} increase and thus the tilt mode is stabilized for a high β_{sp}. On the other hand, a meandering, cycling ion spends most of its time inside the separatrix. If the tilt mode starts to grow for a low β_{sp}, the motion of meandering, cycling ions is synchronized with the tilting motion inside the separatrix. This is the reason why the phase difference between the tilt forces $(\boldsymbol{j} \times \boldsymbol{B})_z^{(1)}$ approaches to zero for a low β_{sp} [Fig. 3.8(b)]. One can speculate that the cycling ions executing a gradient-$\boldsymbol{B}$ drift play a role as "chain" to connect the internal plasma with the external plasma and stabilize the tilting motion through their "chain" effect (Fig. 3.10).

Let us discuss the role of an electric field. Figure 3.11 shows the temporal evolutions of an electric field energy for three different values of $\bar{s}$, where the energy is averaged over the whole volume. The difference between the ion and electron Larmor radii causes the charge separation near the separatrix, thus generating the radial components of an electric field. It is found from Fig. 3.11 that the electric field generated by the finite ion Larmor radius effect becomes larger as $\bar{s}$ decreases. However, the generated field is dominated by the radial component and so it causes merely the $\boldsymbol{E} \times \boldsymbol{B}$ drift which rotates the FRC plasma about the symmetric axis.

A number of experimental evidences [45] indicate that a FRC plasma tends to relax into the hollow current profile which is stable against the tilt mode. Incidentally, we have observed that the current profile becomes hollow near the field-null line in the early phase

of the simulation. However, the change of current profile is limited to a narrow region near the field-null line and so this effect in the tilt stabilization is expected to be small. The comparison of the simulation results with the experimental ones is not straightforward, because a transport mechanism may play a role in the profile relaxation and the hollow profiles exist in the relatively small X_s ($0.3 < X_s < 0.65$) and high β_{sp} plasmas [45]. Moreover, the observed FRC plasma have a tendency to rotate about the symmetric axis which gives rise to the rotational instability [11]. These situations are different from our model.

Table 3.1: Characteristics of equilibrium solutions used in particle simulations, including beta value at separatrix, β_{sp}; hollowness parameter, D; kinetic effect parameter, $\bar{s}$; ratio of separatrix to vessel radius, X_s; elongation, E; normalized growth rate, γ/γ_M.

RUN	β_{sp}	D	$\bar{s}$	X_s	E	γ/γ_M
R1	0.02	−0.6	3.0	0.841	2.14	0.58
R2	0.10	−0.6	3.0	0.798	2.27	0.20
R3	0.20	−0.6	3.0	0.739	2.44	0.02
R4	0.02	−0.6	2.0	0.841	2.14	1.00
R5	0.02	−0.6	5.0	0.841	2.14	0.93
R6	0.02	0.4	3.0	0.742	2.46	0.63
R7	0.10	0.4	3.0	0.709	2.53	0.33
R8	0.02	0.0	3.0	0.802	2.26	0.54
R9	0.10	0.0	3.0	0.760	2.39	0.21
R10	0.02	0.4	2.0	0.742	2.46	0.70

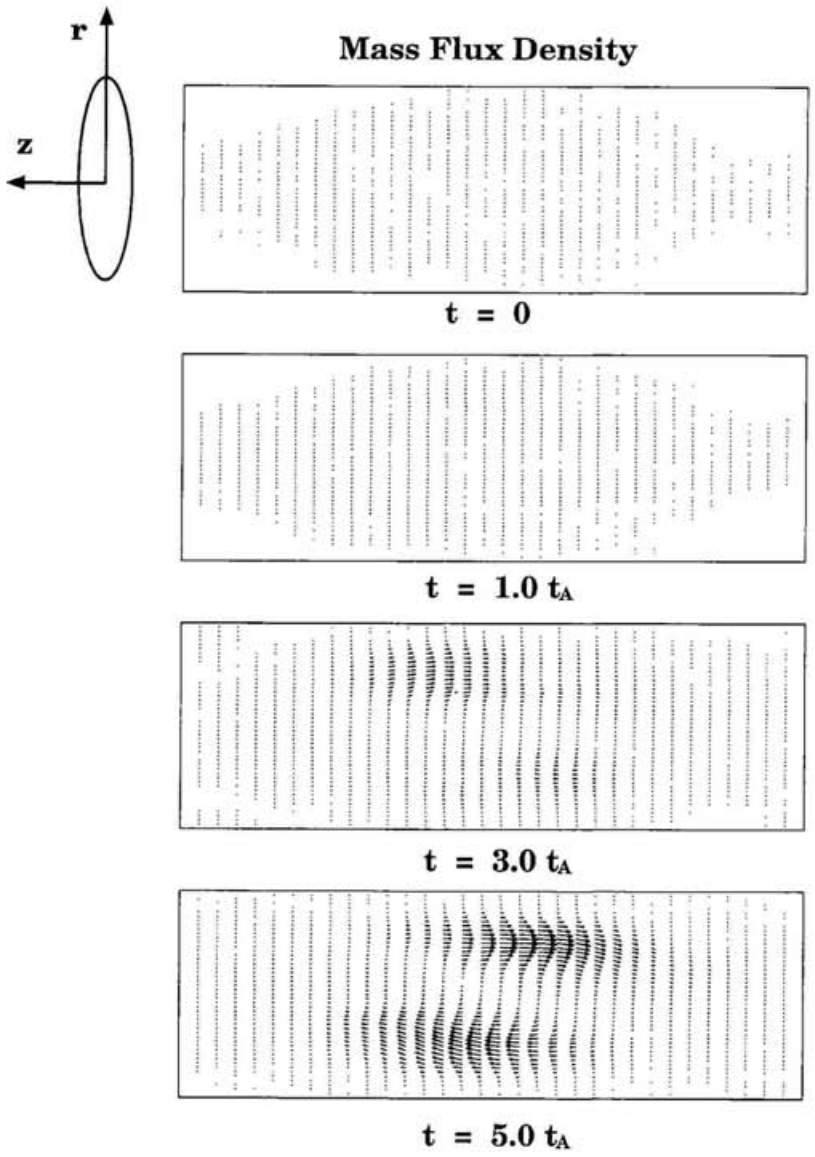

Figure 3.1: Vector plots of mass density flux in the poloidal cross section at the periods of $t/t_A = 0.0$, 1.0, 3.0, and 5.0 for the case R1.

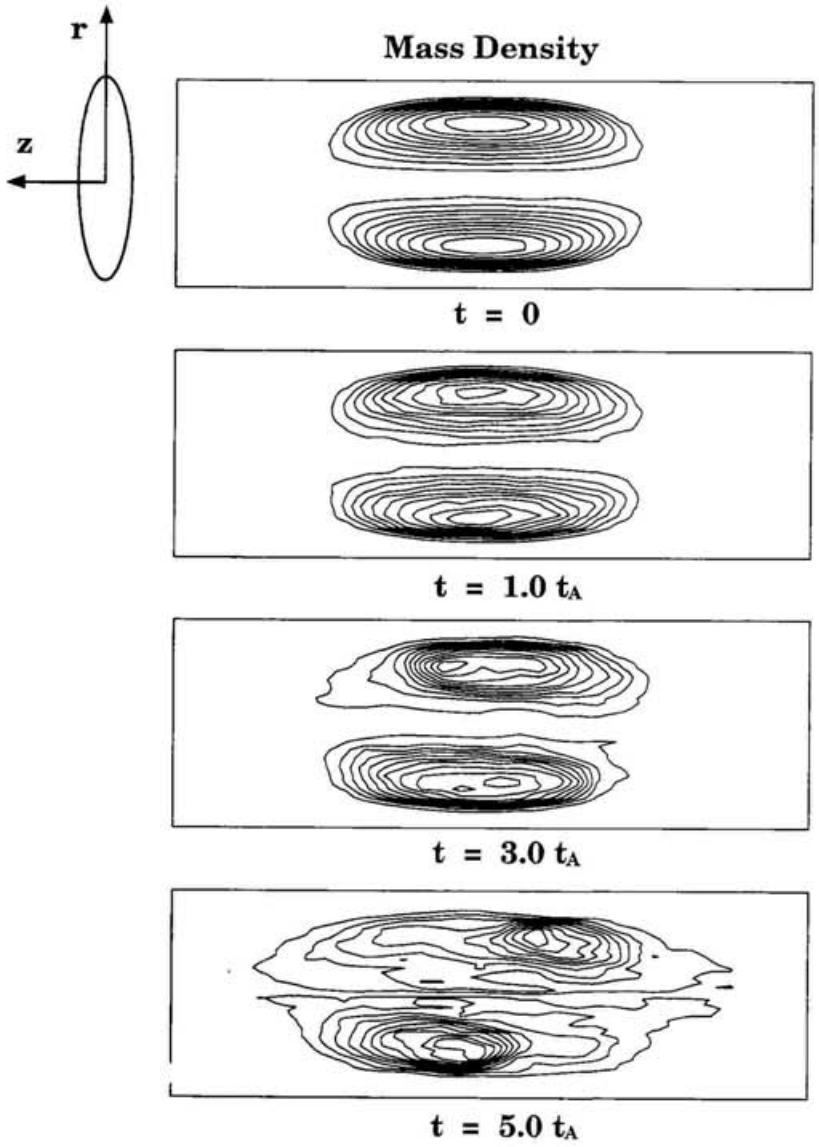

Figure 3.2: Contour plots of mass density for the same case as Fig. 3.1.

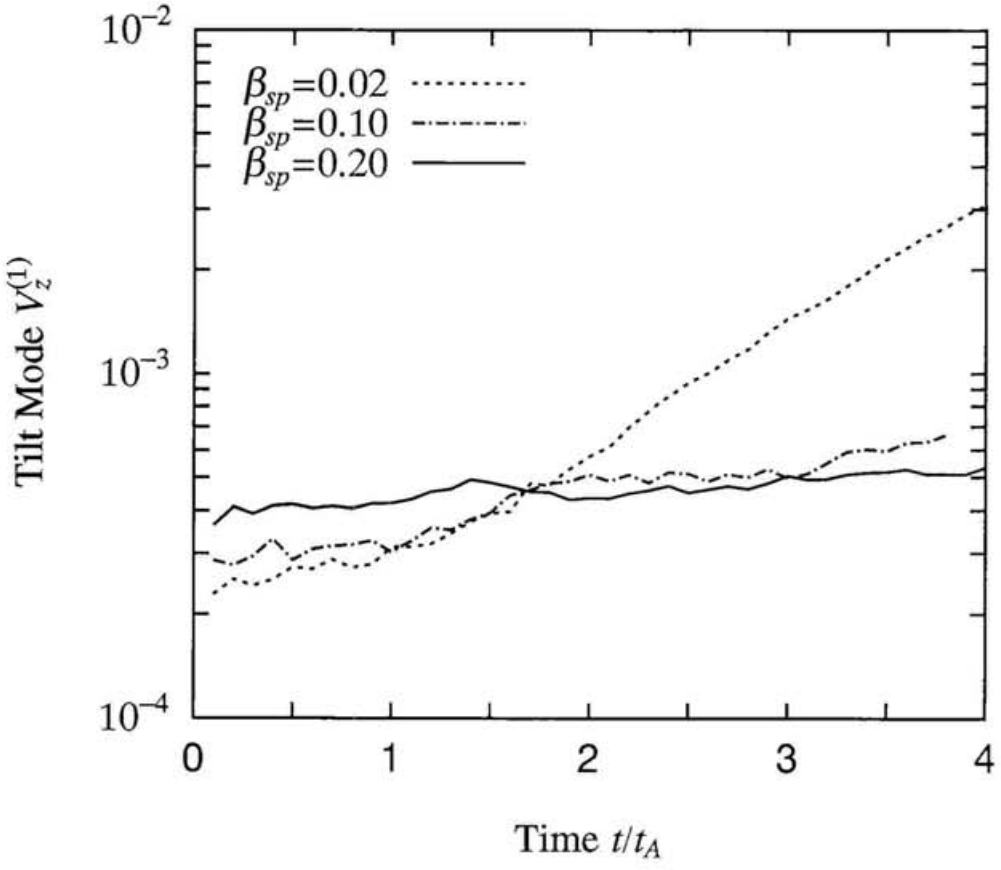

Figure 3.3: Time history of the tilt mode amplitude $V_z^{(1)}$ for three different values of β_{sp}, i.e., $\beta_{sp} = 0.02$(R1), 0.10(R2), and 0.20(R3).

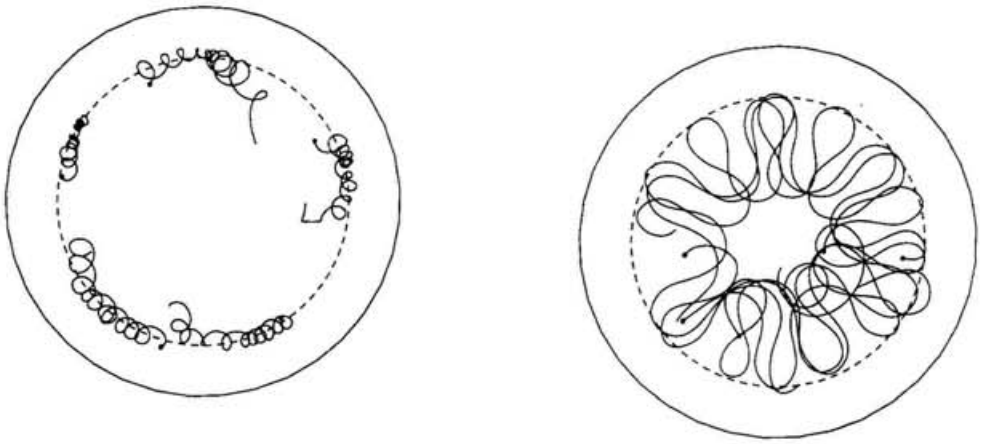

(a) **(b)**

Figure 3.4: The typical orbits of cycling ions projected on the midplane for the case R3 where (a) five gradient-B drift orbits and (b) five meandering orbits are displayed. The solid and broken circles stand for the conducting wall and the magnetic separatrix, respectively. Each curve represents the ion trajectories during four Alfvén transit times from the start of simulation and a closed circle is attached to each curve to show the starting point.

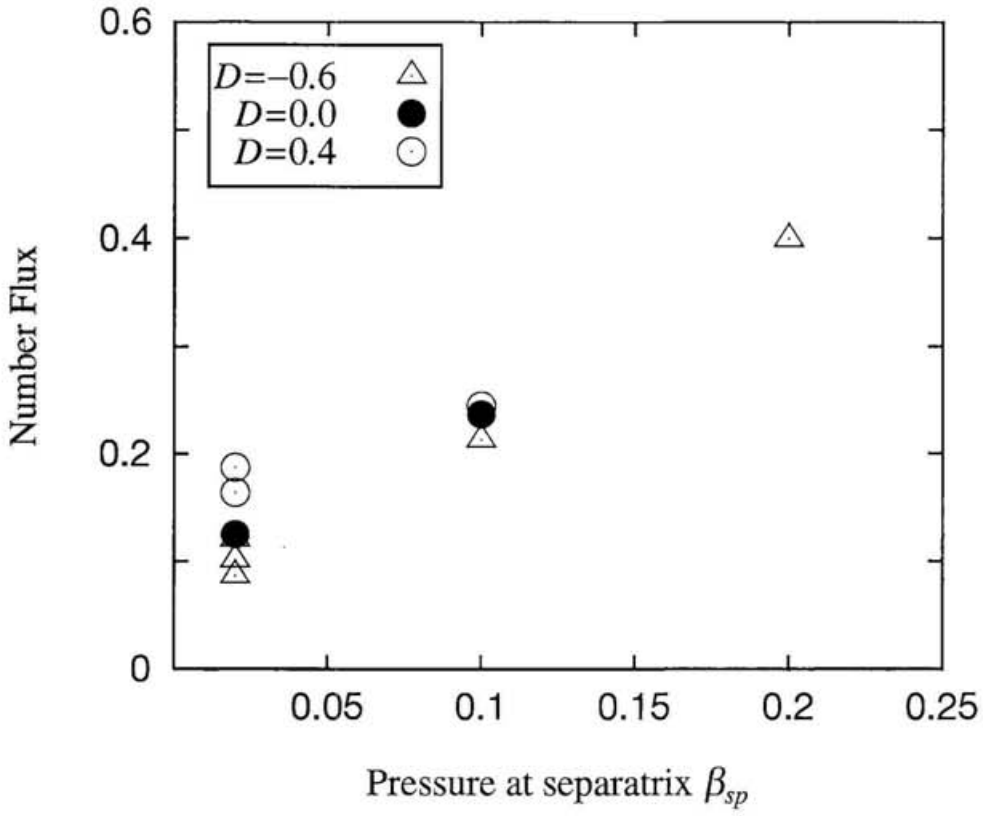

Figure 3.5: The average number flux of the cycling ions normalized by total number of ions as a function of β_{sp} for all cases where open triangles, closed circles, and open circles correspond to the parameter $D = -0.6$, 0.0, and 0.4.

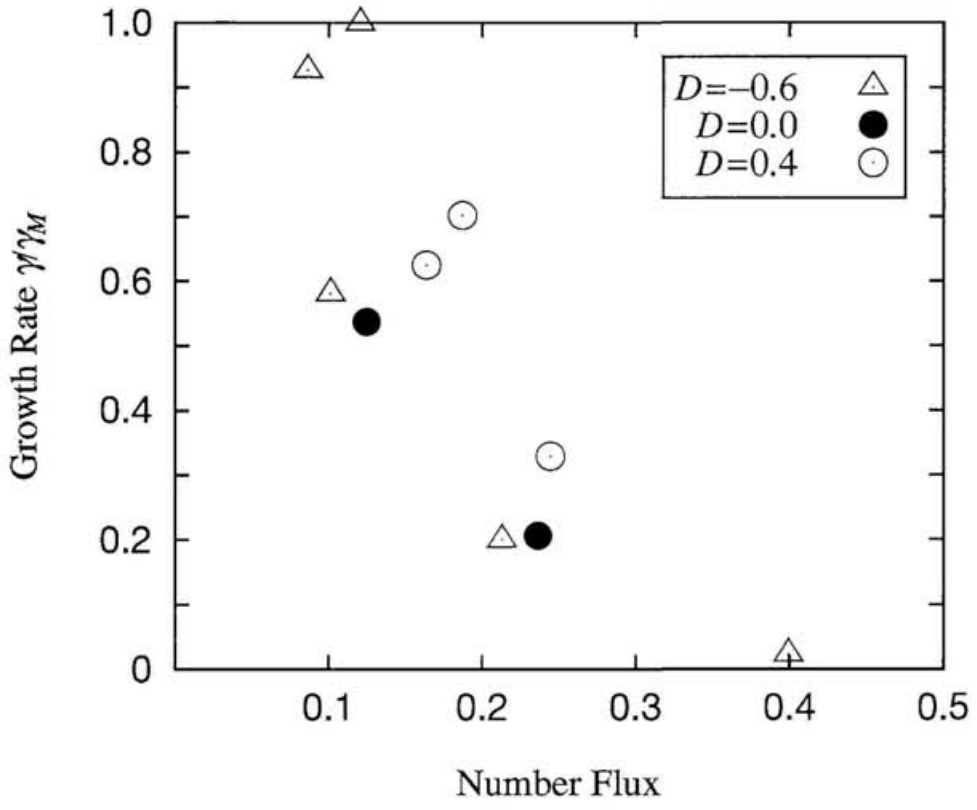

Figure 3.6: Tilt growth rates as a function of average number flux of cycling ions normalized by total number of ions for the same cases as Fig. 3.5.

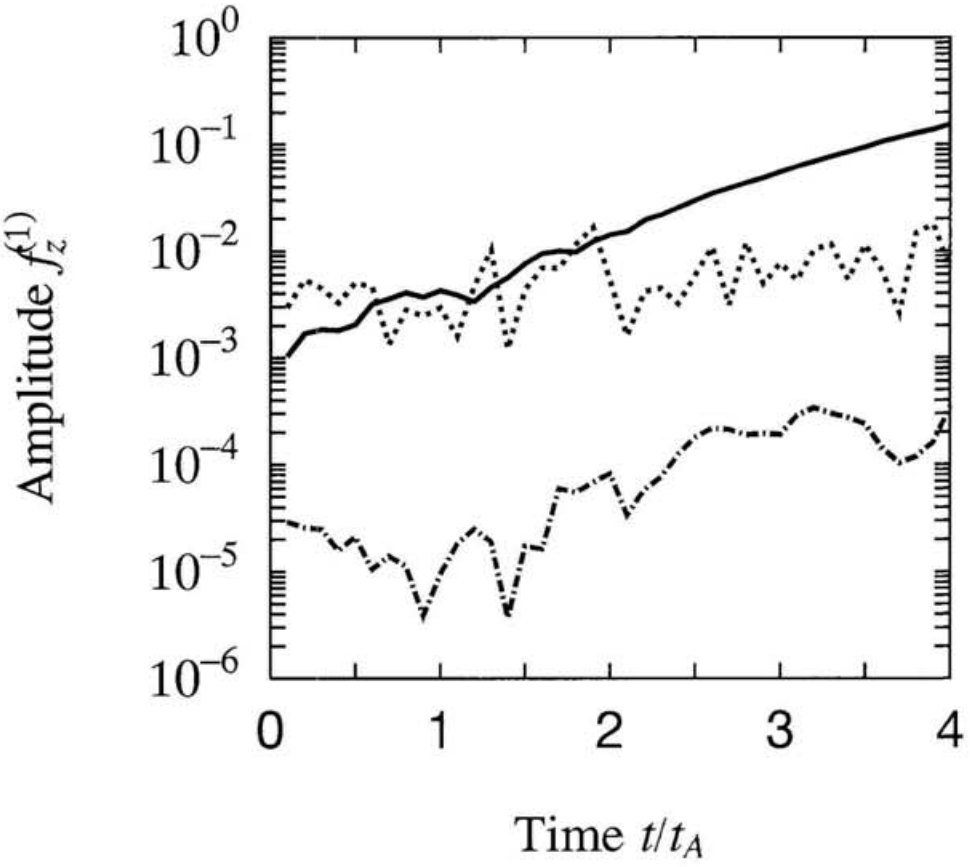

Figure 3.7: Time history of three components of the tilt force for the case R1 in Table 3.1, where the solid, dotted, and dot-dashed lines stand for $j \times B$, ρE, and ∇P, respectively.

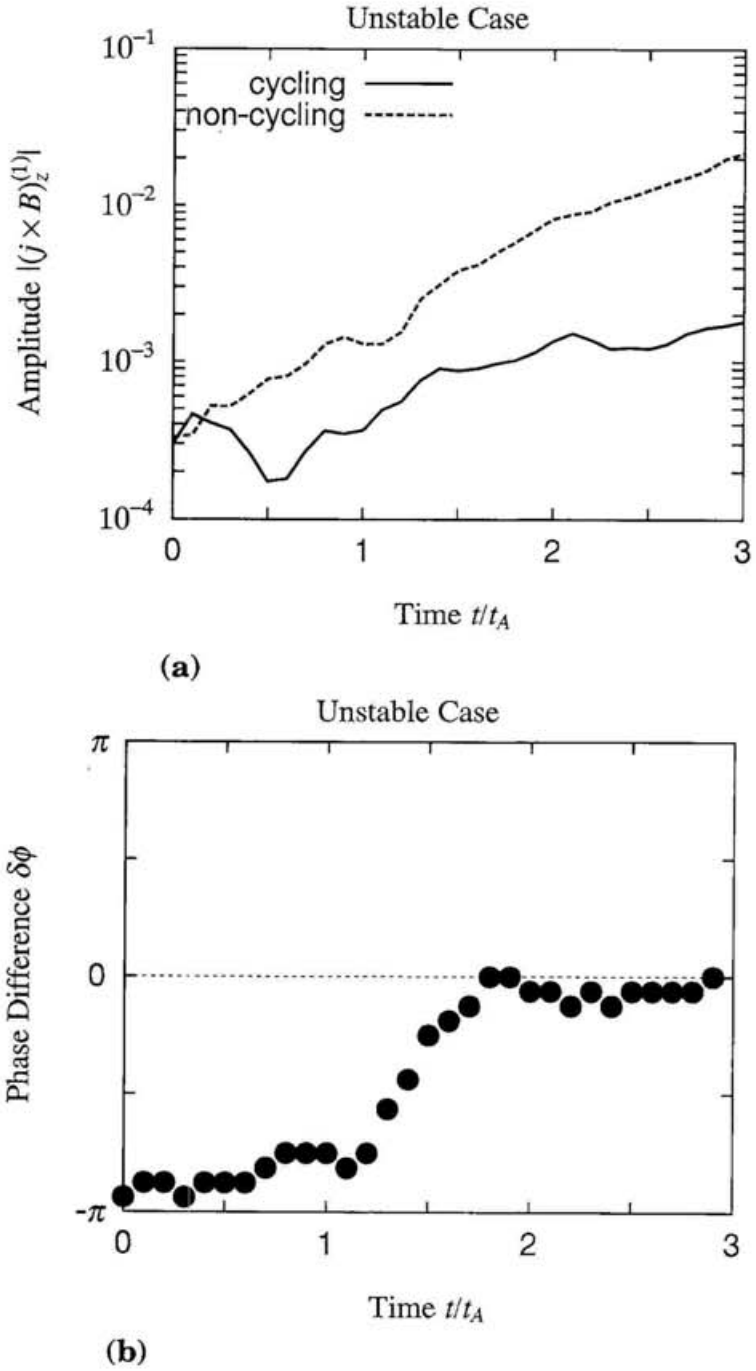

Figure 3.8: Time histories of (a) the amplitudes of the tilt forces acting on cycling ions and non-cycling ions, and (b) their phase difference for the unstable case R4.

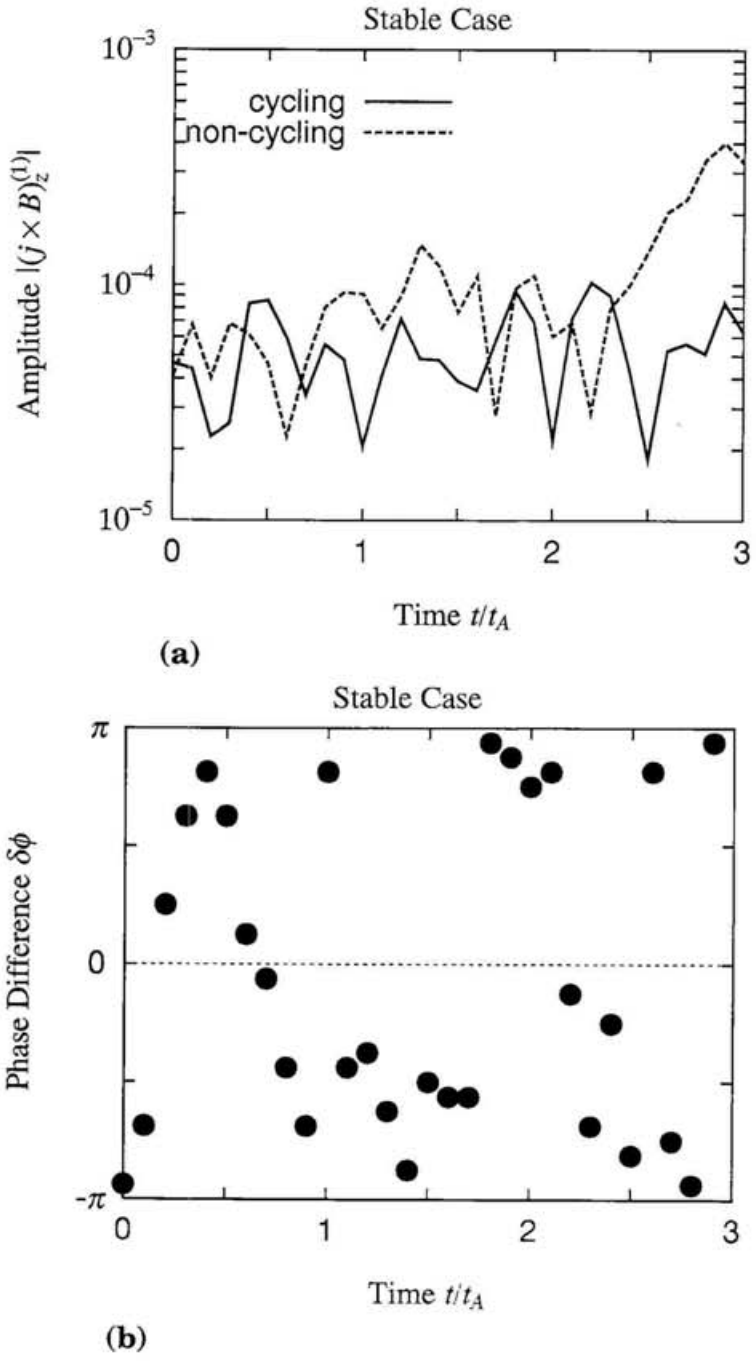

Figure 3.9: The same figure as Fig. 7 but for the stable case R3.

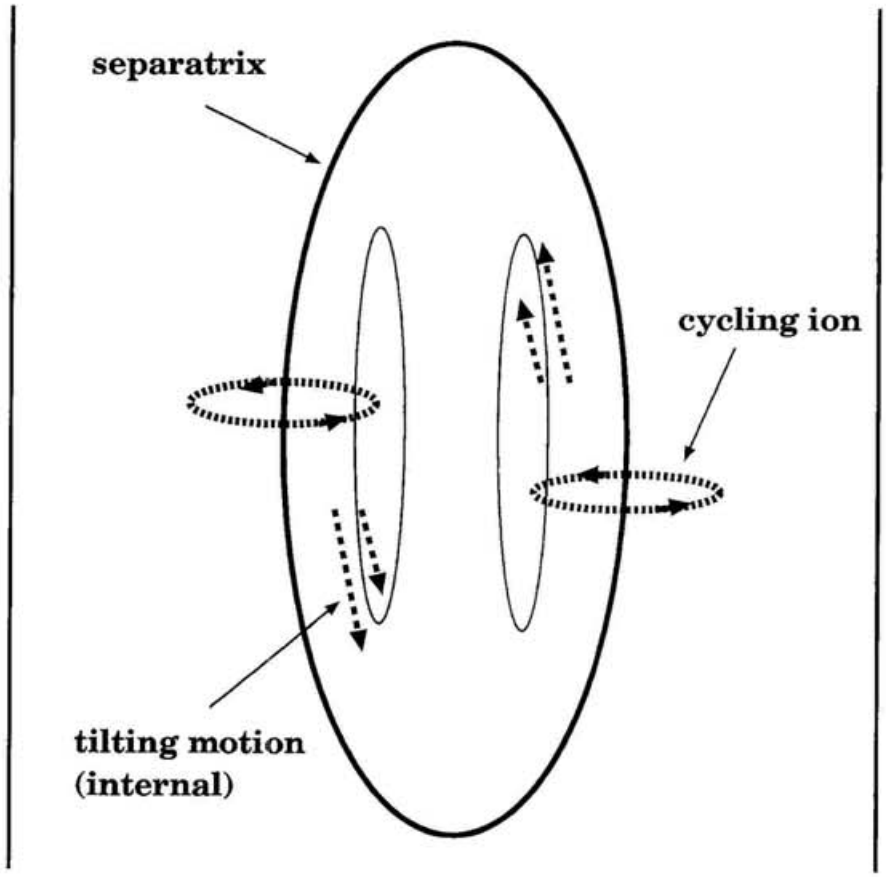

Figure 3.10: Schematic diagram of chain effect by cycling ions. Collective motion is generated inside the separatrix as a result of the excitation of tilt instability. Cycling ions play a role to connect the unstable internal plasmas with stable external plasmas and keep the system stable against the tilt instability.

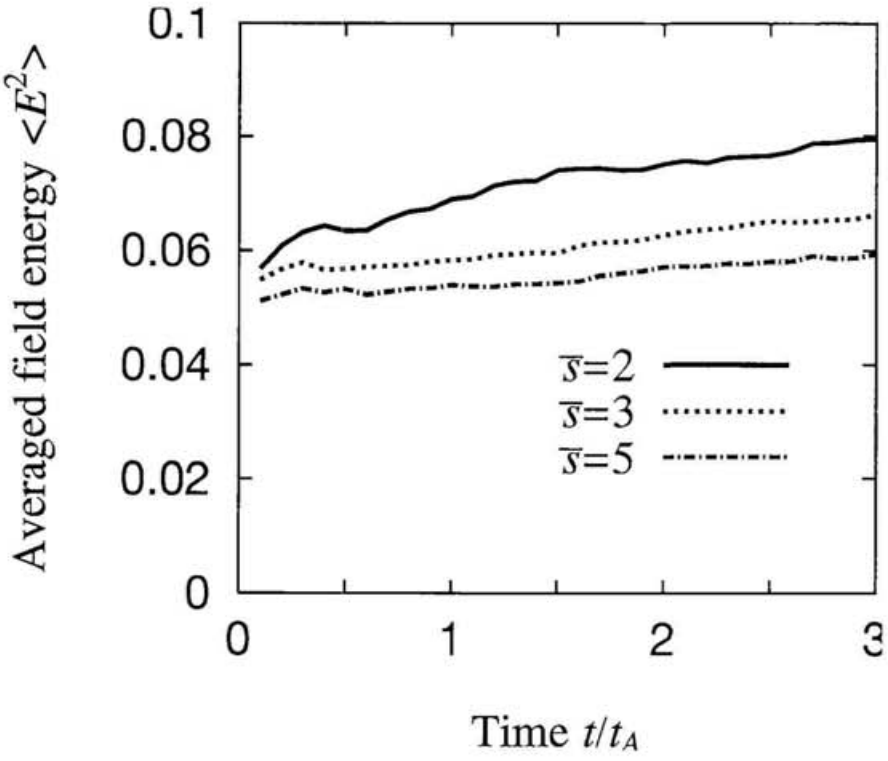

Figure 3.11: Time history of an average electric field for three different values of $\bar{s}$, i.e., $\bar{s} = 2.0$(R4), 3.0(R1), and 5.0(R5).

3.2 Stabilization by energetic beam ions

The previous studies [55,56] show that the beam components in a FRC plasma can play an important role to suppress the tilt instability. The purpose of this section is to investigate the role of beam ions by carrying out the particle simulation. There are two important parameters which we may change independently in this simulation. One is the ratio of the beam current to the thermal plasma current I_b/I_p, and the other is the ratio of the number of beam ions to the number of thermal ions N_b/N_i. What we want to clarify is which plays an important role in the suppression of tilt mode, the magnitude of beam current or the total amount of kinetic energy of beam ions. Because the total current and total kinetic energy (ϵ_{Kb}) of beam ions are roughly given by $I_b \sim N_b v_b$ and $\epsilon_{Kb} \sim N_b v_b^2/2 \sim I_b^2/2N_b$, we can evaluate the dependences of the tilt instability on I_b and ϵ_{Kb} by controlling two parameters I_b/I_p and N_b/N_i. If the current ratio I_b/I_p changes with keeping the number ratio N_b/N_i constant, it means that the ratio of the beam velocity to the thermal velocity v_b/v_{Ti} changes. On the other hand, if the number ratio changes with keeping the ratio $(I_b/I_p)/(N_b/N_i)$ constant, it roughly means that the velocity ratio v_b/v_{Ti} is constant. We fix the kinetic parameter $\bar{s}$ to 3, the profile parameter β_{sp} to 0.02, and the hollowness parameter D to -0.6 for all cases. These values of three parameters promote the tilt mode to be unstable for no beam case, as we have seen in the previous section.

3.2.1 Fixed number case for beam ions

Ten simulation runs are carried out and they are classified into two types. One type is used to investigate the dependence of the tilt mode on the velocity of the beam ions with keeping the total number of beam ions constant (RB1~RB6 in Table 3.2), and the other

type is to investigate the dependence on the total number of beam ions with keeping the ratio $(I_b/I_p)/(N_b/N_i)$ constant (RB7~RB10 in Table 3.3).

First, let us describe the ion density distribution in the real space. Figure 3.12(a) shows the contour plots of thermal ion density (left side) and beam density (right side) in the poloidal cross section at the time of $t/t_A = 0$ for the case RB2. The beam density distribution is determined according to the Eq. (2.52) in Sec. 2.2. Figure 3.12(b) displays the radial distributions of the densities on the midplane, where the density is normalized by that of thermal ions in the field-null line. It is clear that the peak of ion distribution exists in the vicinity of the field-null line. We start the particle simulation from such configurations.

Figure 3.13 shows the orbits of arbitrary five beam ions during 5 Alfvén times for the case RB1 of Table 3.2. The yellow ellipsoid represents the magnetic separatrix on each figure. The top panel shows the side view of the orbits and the bottom panel shows the projection of the orbits onto the midplane. It is found that the stable orbits of beam ions exist near the field-null line on the midplane and undergoes the small oscillation in the radial and axial directions. Most of the other beam ions occupy the same region in the vicinity of the field-null line.

The development of tilt instability is defined in terms of the Fourier amplitude of $n = 1$ mode of the axial fluid velocity $V_z^{(1)}(t)$. We carried out the several simulation runs to investigate the dependence of the tilt mode on the parameter I_b/I_p. The important physical quantities used for the simulation are listed in Table 3.2, where the tilt growth rate γ is normalized by Alfvén transition time defined by both the vessel radius and the Alfvén velocity associated with the magnetic field at the vessel wall and the ion density at the field-null. Since the number ratio N_b/N_i is fixed to 0.01 in these cases, the velocities

of beam ions increase with increasing I_b/I_p. The relation between the tilt growth rate and the current ratio is presented in Figure 3.14. From this figure, it is found that the growth rate remains almost the same as that for no beam case (R1) for $0 < I_b/I_p < R_c(\sim 0.03)$. If the current ratio exceeds this critical value R_c, the larger the current ratio is, the smaller the tilt growth rate becomes. The physical meaning of R_c will be discussed in the next paragraph. Figure 3.15 shows the relation between the tilt growth rate and the kinetic energy ratio of total beam ions to total thermal plasmas for the same cases as Fig. 3.14. It reveals that the ion beam needs more than 30% of the kinetic energy of thermal ions to reduce the growth rate below a half of that for no beam case.

Table 3.2 shows that the tilt stabilization becomes more efficient as the beam velocity increases. Let us introduce the dimensionless parameter $\bar{s}_{eff}$ to evaluate the beam stabilization effect in the similar way to the definition of $\bar{s}$. That is, $\bar{s}_{eff}$ is given by replacing the thermal velocity in the definition of $\bar{s}$ by the average velocity of the total ions as,

$$\bar{s}_{eff} = \frac{m_i c}{r_{sp} q_i} \int_R^{r_{sp}} \frac{r dr}{\langle v_i \rangle B_z(r)} , \tag{3.7}$$

where m_i and q_i are the mass and the charge of ions, respectively, c is the light velocity, $\langle v_i \rangle$ is the average ion velocity on the midplane, and $B_z(r)$ is the z component of the magnetic field on the midplane. The parameter $\bar{s}$ measures the ratio of the confinement spatial scale to the ion Larmor radius defined by the ion thermal velocity. The difference appears between the parameters $\bar{s}$ and $\bar{s}_{eff}$ as the beam velocity exceeds the ion thermal velocity. Therefore, $\bar{s}$ is not a good parameter to evaluate the kinetic effect of total ions when the beam component with the velocity larger than the ion thermal velocity exists. The relation between $\bar{s}_{eff}$ and the current ratio I_b/I_p is presented in Figure 3.16. It is important to note that $\bar{s}_{eff}$ remains constant ($\bar{s}_{eff} \sim 3$) when the current ratio I_b/I_p is less than the critical value R_c. If the current ratio I_b/I_p exceeds the critical value R_c,

$\bar{s}_{eff}$ becomes small with increasing I_b/I_p. In other words, the critical current ratio R_c corresponds to the point at which $\bar{s}_{eff}$ starts to deviate from the normal $\bar{s}$ value.

Figure 3.17 displays the relation between the tilt growth rate and the parameter $\bar{s}_{eff}$. The tilt growth rate becomes small as $\bar{s}_{eff}$ decrease below $\bar{s}$ $(= 3)$, and there exists a clear linear relation between γ and $\bar{s}_{eff}$. Thus, the tilt stabilization effect of the ion beam can be evaluated in terms of the parameter $\bar{s}_{eff}$ value for the case where the velocity of beam ions varies.

3.2.2 Fixed velocity case for beam ions

We discuss the dependence of the tilt instability on the number ratio N_b/N_i in this subsection. The parameters used for the simulation are listed in Table 3.3. The ratio $(I_b/I_p)/(N_b/N_i)$, which roughly stands for the ratio of beam velocity to ion thermal velocity, is fixed to 2.2. It follows from this choice that the velocity of beam ions exists in the limited range of $3.0 < v_b/v_{Ti} < 4.0$.

The relation between the tilt growth rate and the current ratio are shown in Fig. 3.18. It is also found, as we have seen, that the growth rate nearly remains the same as that for no beam case (R1) for $0 < I_b/I_p < R_c(\sim 0.03)$, and it starts to decreases as soon as I_b/I_p exceeds R_c. This tendency is exactly the same as we have obtained for the case where the velocity of beam ions varies. In other words, the influence of beam ions on the tilt growth rate can be evaluated by the current ratio I_b/I_p regardless of whether the velocity of ion beams varies or the number of ion beams varies. This effect becomes remarkable as the current ratio increases more than R_c.

Figure 3.19 shows the dependence of $\bar{s}_{eff}$ on the current ratio I_b/I_p for the same case as Fig. 3.18. Since the number ratio changes with keeping the beam velocities constant,

the averaged velocity of ions does not increase largely with increasing the current ratio consequently, the growth rate varies independently of the parameter $\bar{s}_{eff}$, as is seen in Fig. 3.20. In other words, $\bar{s}_{eff}$ is not a suitable parameter to evaluate the beam stabilization effect when the number ratio N_b/N_i varies.

Next we examine the relation between the tilt growth rate and the kinetic energy ratio of total beam ions to total thermal plasma. The result is presented in Fig. 3.21. It is important to note that the ion beam needs only 15% of the total kinetic energy of thermal ions to reduce the growth rate below a half of that for no beam case. On the contrary to the fixed number case where it needs more than 30% of the energy (see Fig. 3.15). These results lead us to the conclusion that the tilt mode can be suppressed more effectively by increasing the number ratio N_b/N_i than increasing the velocity ratio v_b/v_{Ti} from a viewpoint of kinetic energy.

Let us examine the driving force of the tilt instability $(\boldsymbol{j} \times \boldsymbol{B})_z^{(1)}$ in order to elucidate the beam stabilization mechanism. For this, we expand the current density into the beam component $\boldsymbol{j}^{(b)}$ and the thermal component $\boldsymbol{j}^{(t)}$ and calculate the two components of the driving force. The definitions of the average amplitude $F^{(\alpha)}(t)$ and the phase difference $\delta\phi$ between two components were expressed in Eq.(3.6),(3.6), where the superscript (α) denotes a beam component $(\alpha = b)$ or a thermal ion component $(\alpha = t)$ in this case. Figure 3.22 shows the time evolutions of the amplitudes for the cases RB7 ($N_b/N_i = 0.005$), RB1 ($N_b/N_i = 0.01$), RB9 ($N_b/N_i = 0.02$) where top and bottom panels represent the force amplitudes acting on the thermal component $[\boldsymbol{j}^{(t)} \times \boldsymbol{B}]_z^{(1)}$ and that acting on the beam component $[\boldsymbol{j}^{(b)} \times \boldsymbol{B}]_z^{(1)}$, respectively. In these cases, the tilt growth rate decreases with increasing the number ratio. There is no obvious difference between three cases as far as the force acting on thermal component concerns [Fig. 3.22(a)]. It is clear that the

force acting on the beam component increases with increasing the number of beam ions. Figure 3.23 shows the time evolutions of the phase difference for three different number ratios, i.e., (a) $N_b/N_i = 0.005$ (RB7), (b) $N_b/N_i = 0.01$ (RB1), and (c) $N_b/N_i = 0.02$ (RB9). It is found that the phase difference remains nearly equal to zero in the case of $N_b/N_i = 0.005$ [Fig. 3.23(a)], i.e., the directions of two forces are almost the same. Thus, beam component of the $(\boldsymbol{j} \times \boldsymbol{B})_z^{(1)}$ force works synchronously so that the tilt instability grows on the whole. In the case of $N_b/N_i = 0.01$ [Fig. 3.23(b)], it can be seen that the phase difference becomes a little large ($\delta\phi \sim \pi/2$). The phase difference almost takes the maximum value ($\delta\phi \sim \pm\pi$) in the case of $N_b/N_i = 0.02$ [Fig. 3.23(c)]. That is to say, the directions of two forces are opposite to each other and the total tilting force becomes weak. Thus, we can conclude that the beam ions play an important role to cancel the tilting motion of the thermal plasma.

3.2.3 Summary and discussions

We have examined the dependences of tilt instability on the ion beam effect by carrying out two types of simulation runs. The first type is the case where the beam velocity varies while keeping the total number of beam ions constant. The second is the case where the total number of beam ions varies while keeping the beam velocity almost constant. In both cases, the growth rate remains almost unchanged until the current ratio I_b/I_p reaches the critical value R_c, and then it gradually decreases as the ratio increases above R_c. The dependences of the growth rates on the current ratio I_b/I_p are exactly the same for both the fixed number case and the fixed velocity case. That is to say, we can evaluate the ion beam effect universally with use of the current ratio.

On the other hand, it is also possible to evaluate the differences between two cases

with use of the kinetic energy ratio. In the case where the velocity of beam ions varies, the ion beam needs 30% of the kinetic energy of the thermal ions to reduce the growth rate below a half of that for no beam case. In the case where the total number of beam ions varies, only 15% of the kinetic energy of thermal ions is needed for beam ions to get the same growth rate. Thus, we come to the conclusion that the tilt mode can be suppressed more effectively by increasing the number of beam ions.

Barnes and Milroy [56] investigated the same problem with using the three-dimensional hybrid simulation code, in which the beam ion and the background plasma are treated as a particle and MHD fluid, respectively. Since the beam ions are injected gradually into the MHD plasma as time elapses, the equilibrium configuration of background plasma is changed markedly after a few Alfvén times. They came to the conclusion that the tilt mode can be stabilized with ion beams whose energy is about 40% of the total kinetic energy which corresponds to more than 60% of the thermal plasma energy. This value is not realistic from the viewpoint of experiments. Furthermore, we note again that the kinetic energy ratio is not appropriate parameter in evaluating the efficiency of tilt suppression.

Table 3.2: Characteristics of equilibrium solutions used in particle simulations, including ratio of number, N_b/N_i; ratio of current, I_b/I_p; ratio of kinetic energy, $\epsilon_{Kb}/\epsilon_{Kp}$; velocity ratio of beam to thermal ion, v_b/v_{Ti}; ratio of separatrix to vessel radius, X_s; elongation, E; growth rate normalized by Alfvén transition time, γ.

RUN	N_b/N_i	I_b/I_p	$\epsilon_{Kb}/\epsilon_{Kp}$	v_b/v_{Ti}	X_s	E	γ
R1	0	0	0	0	0.84	2.14	0.563
RB1	0.01	0.022	0.049	3.4	0.86	2.12	0.603
RB2	0.01	0.03	0.099	4.6	0.87	2.08	0.419
RB3	0.01	0.035	0.147	6.0	0.87	2.07	0.545
RB4	0.01	0.04	0.211	7.4	0.88	2.05	0.390
RB5	0.01	0.045	0.301	11.0	0.89	2.08	0.251
RB6	0.01	0.051	0.409	13.2	0.89	2.06	0.192

Table 3.3: Characteristics of equilibrium solutions used in particle simulations, including ratio of number, N_b/N_i; ratio of current, I_b/I_p; ratio of kinetic energy, $\epsilon_{Kb}/\epsilon_{Kp}$; velocity ratio of beam to thermal ion, v_b/v_{Ti}; ratio of separatrix to vessel radius, X_s; elongation, E; growth rate normalized by Alfvén transition time, γ.

RUN	N_b/N_i	I_b/I_p	$\epsilon_{Kb}/\epsilon_{Kp}$	v_b/v_{Ti}	X_s	E	γ
R1	0	0	0	0	0.84	2.14	0.563
RB7	0.005	0.011	0.02	2.9	0.85	2.13	0.567
RB1	0.01	0.022	0.049	3.4	0.86	2.12	0.603
RB8	0.015	0.034	0.08	3.1	0.87	2.09	0.473
RB9	0.02	0.045	0.13	3.8	0.87	2.07	0.263
RB10	0.025	0.055	0.15	3.5	0.88	2.06	0.248

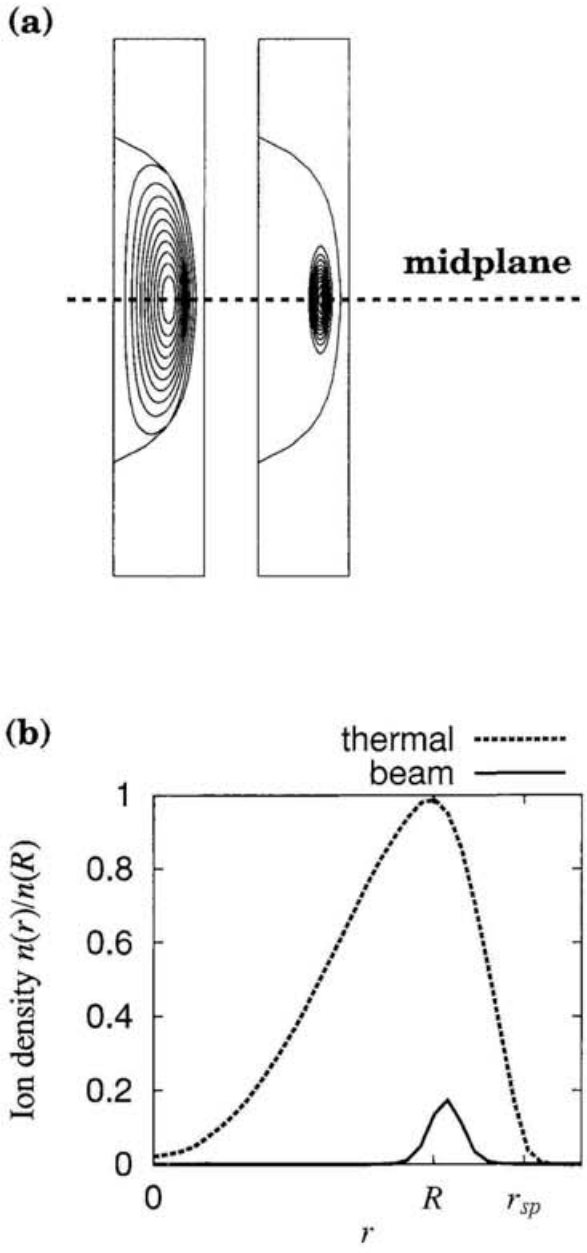

Figure 3.12: Ion distribution function for the case R2 where (a) contour plots of thermal ion density (left side) and beam density (right side) in the poloidal cross section at the initial period, and (b) radial distribution of each ion density on the midplane.

(a)

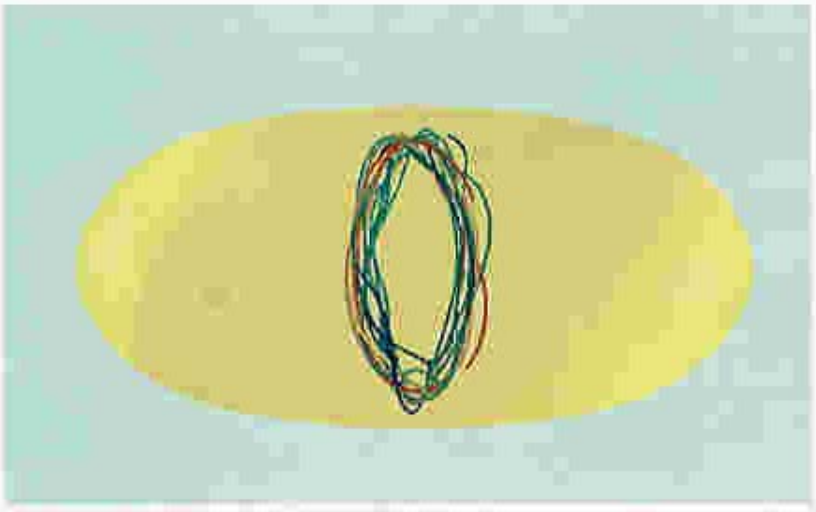

(b)

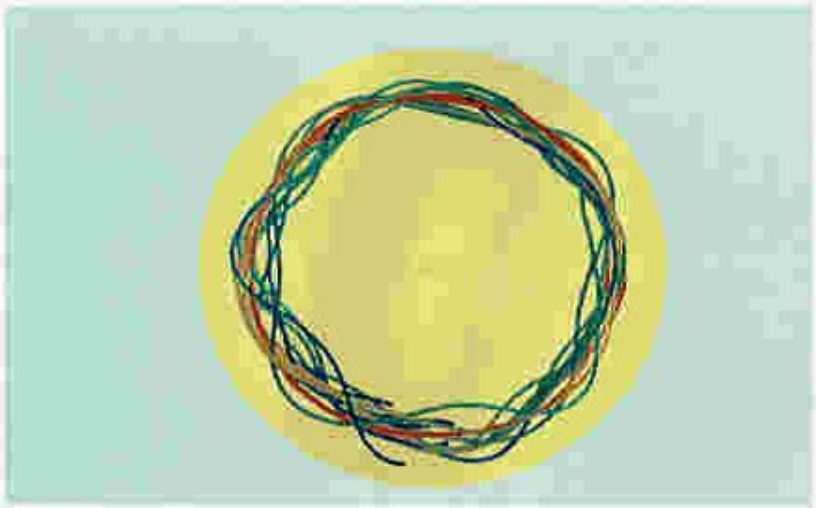

Figure 3.13: The typical orbits of beam ions for the case R1 where the simulation parameters are listed in Table 3.2. Figures (a) and (b) represents side and top views of five orbits, respectively.

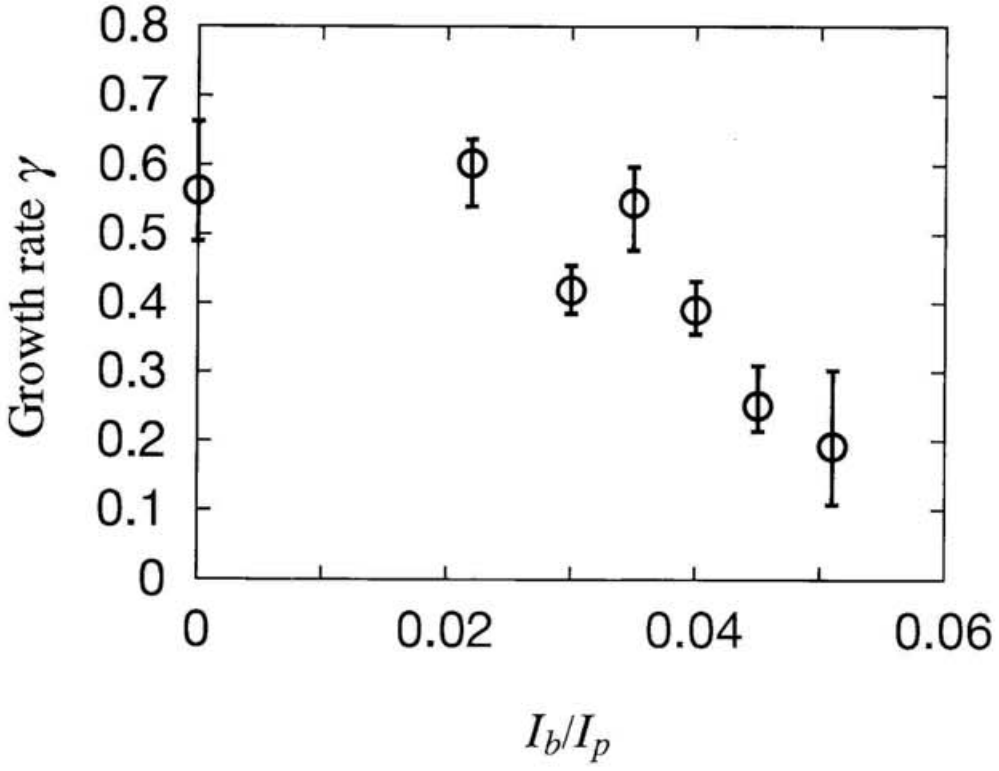

Figure 3.14: Tilt growth rates as a function of the current ratio of beam ions to thermal plasma for the cases where the number ratio N_b/N_i is fixed.

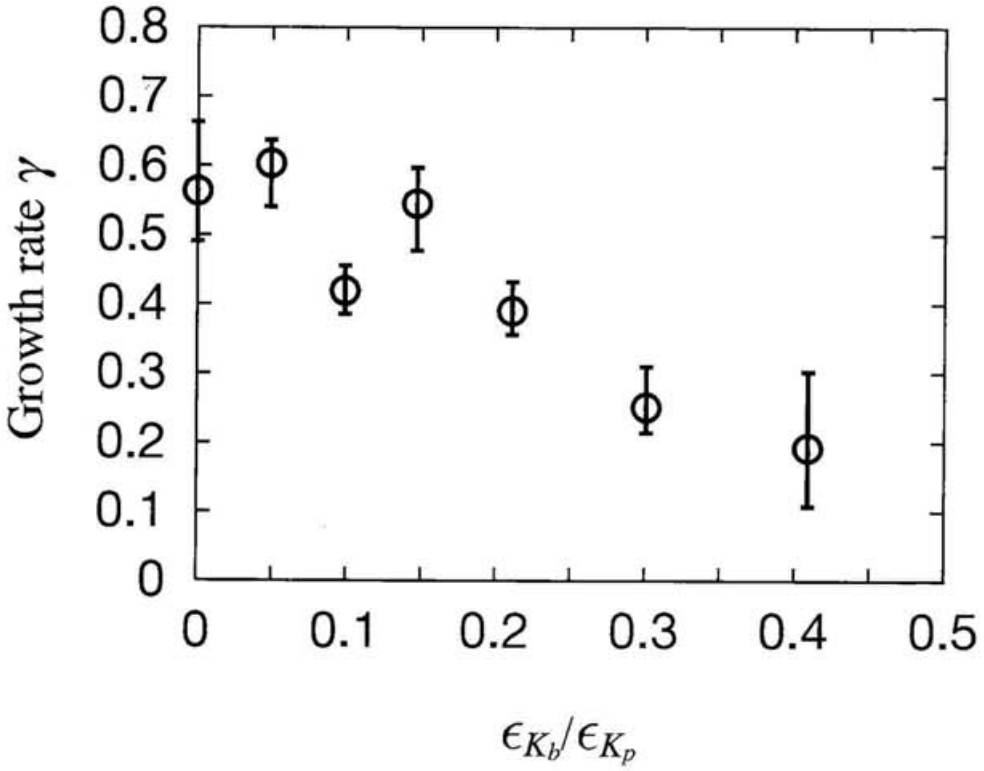

Figure 3.15: Tilt growth rates as a function of the kinetic energy ratio of beam ions to thermal plasma for the same cases as Fig. 3.14.

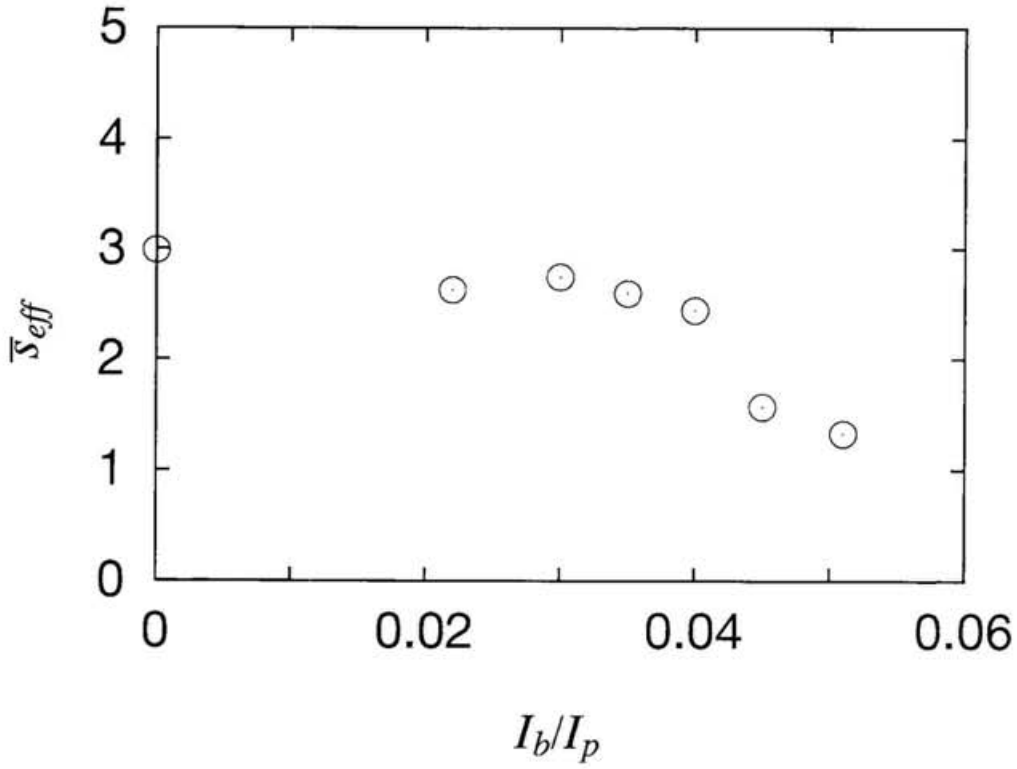

Figure 3.16: The dependence of $\bar{s}_{eff}$ on the current ratio of beam ions to thermal plasma for the same cases as Fig. 3.14.

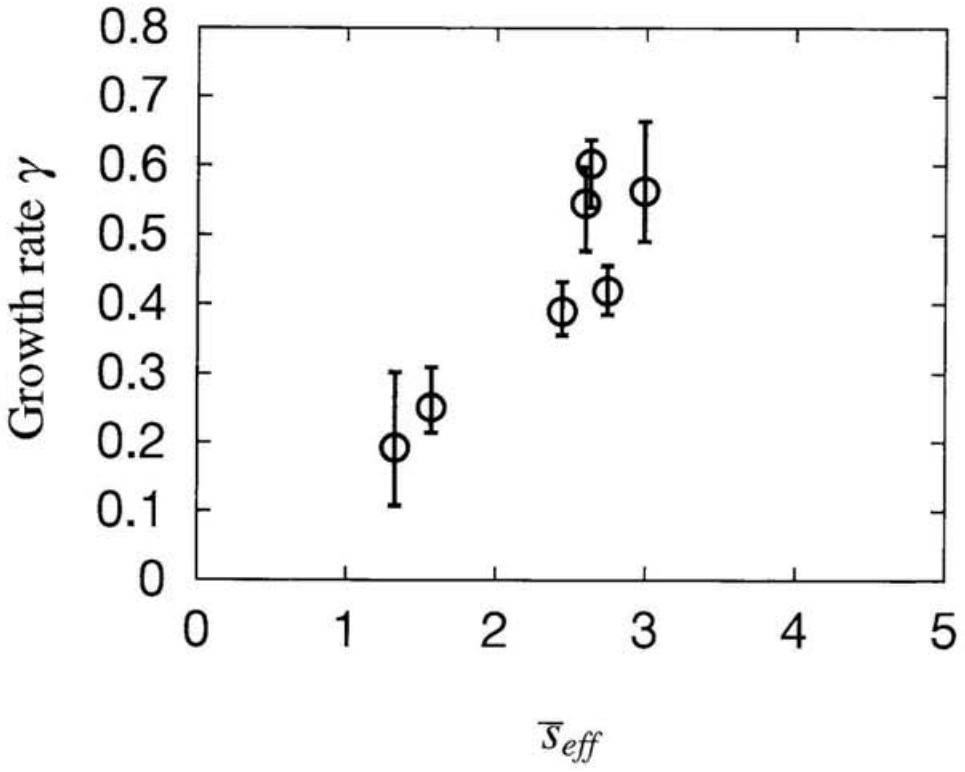

Figure 3.17: Tilt growth rates as a function of $\bar{s}_{eff}$ for the same cases as Fig. 3.14.

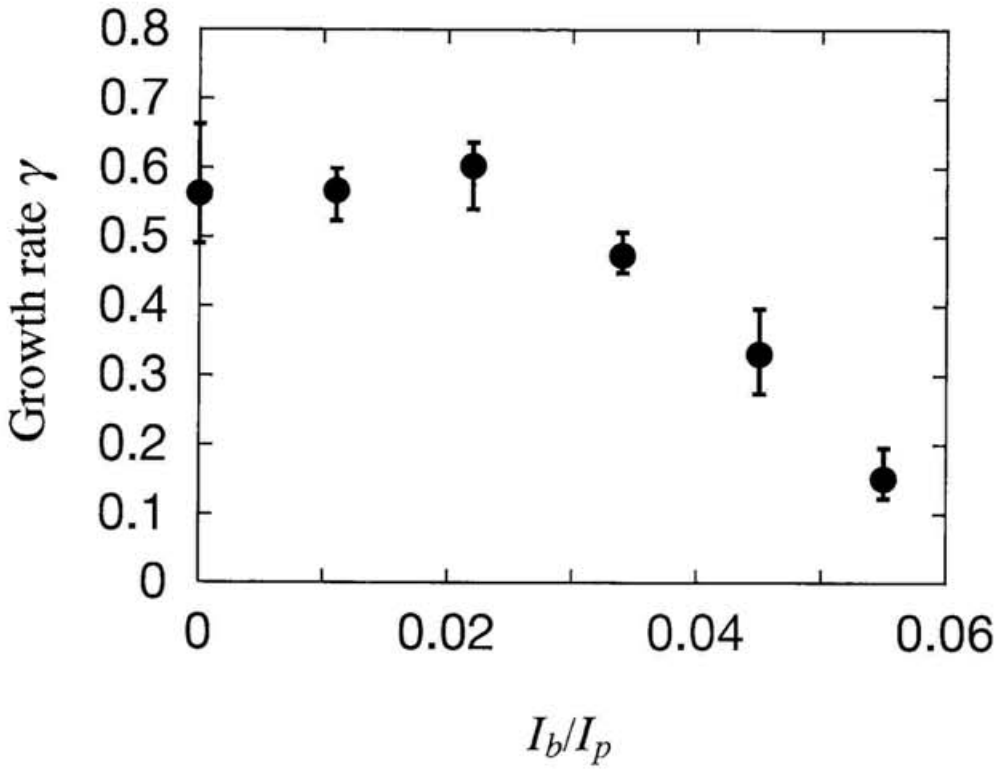

Figure 3.18: Tilt growth rates as a function of the current ratio of beam ions to thermal plasma for the cases where the ratio $(I_b/I_p)/(N_b/N_i)$ is fixed.

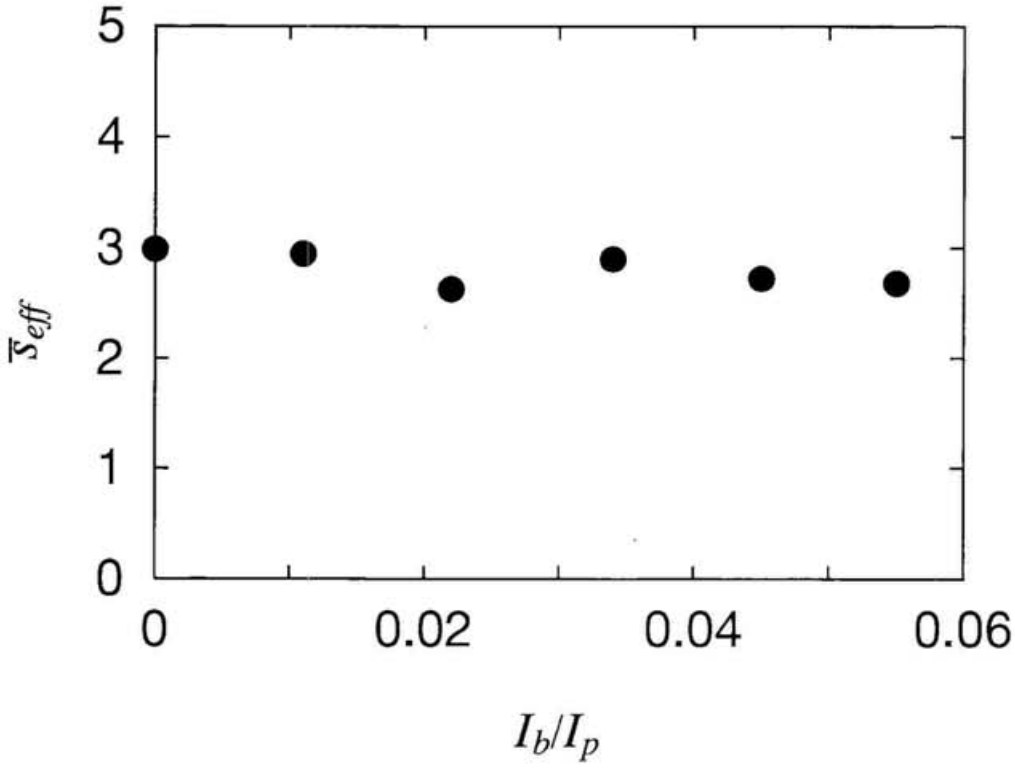

Figure 3.19: The dependence of $\bar{s}_{eff}$ on the current ratio of beam ions to thermal plasma for the same cases as Fig. 3.18.

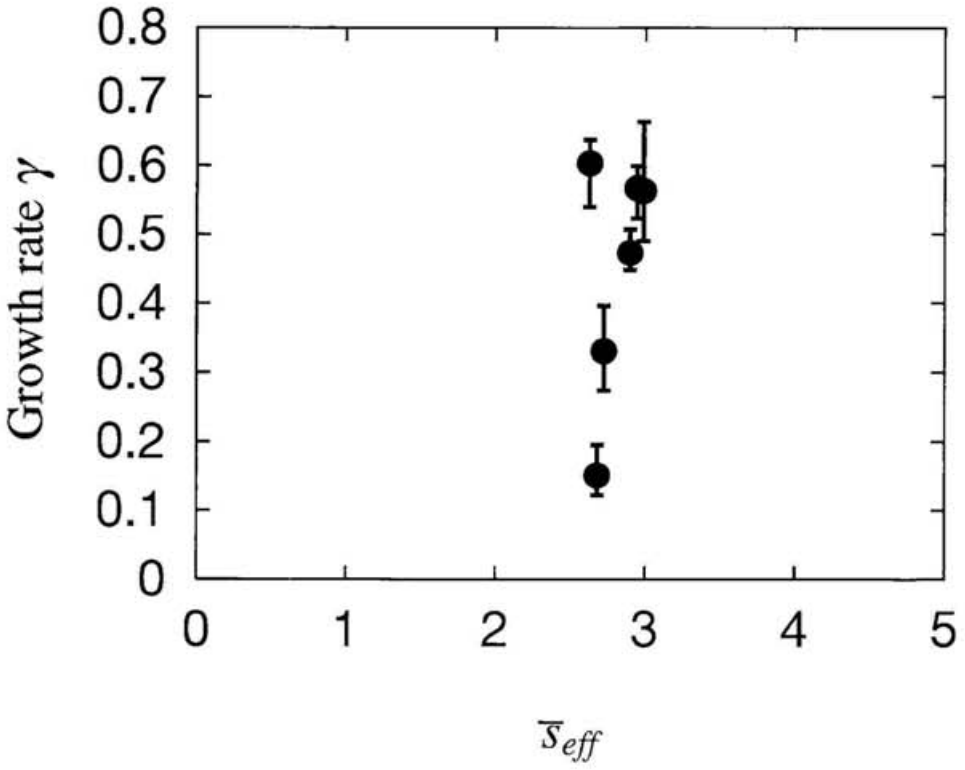

Figure 3.20: Tilt growth rates as a function of $\bar{s}_{eff}$ for the same cases as Fig. 3.18.

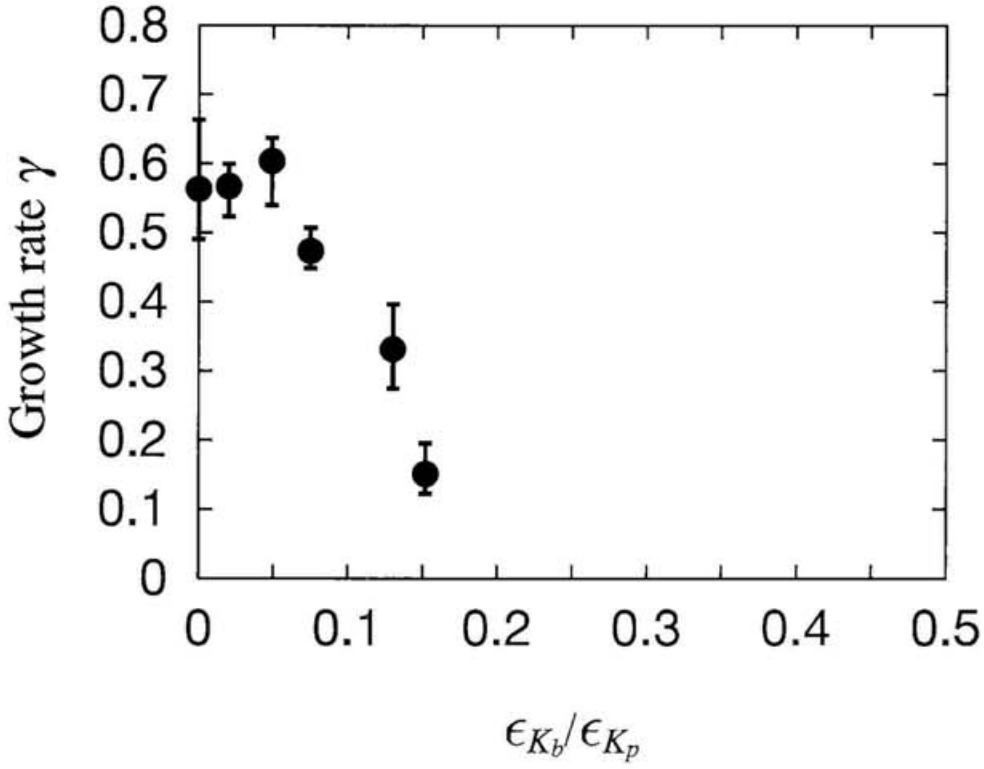

Figure 3.21: Tilt growth rates as a function of the kinetic energy ratio of beam ions to thermal plasma for the same cases as Fig. 3.18.

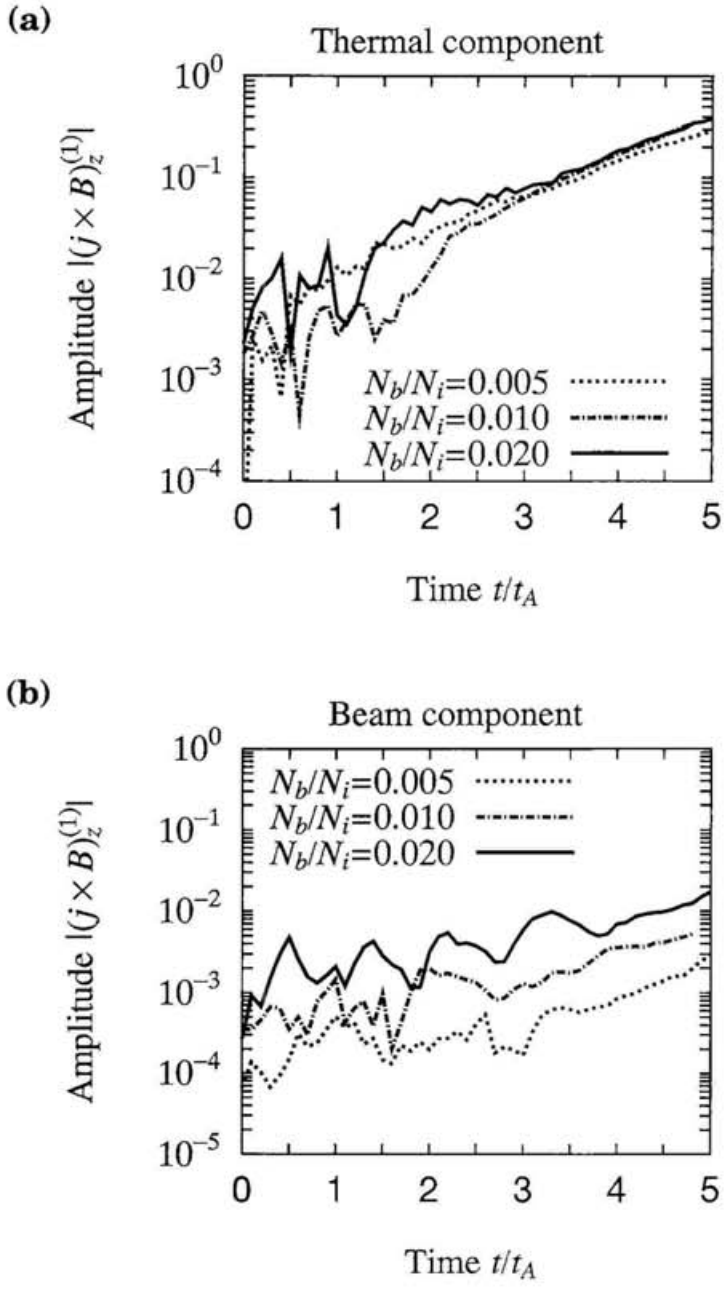

Figure 3.22: Time histories of the amplitudes of the tilt forces acting on (a) background thermal ions, and (b) beam ions for three different values of N_b/N_i.

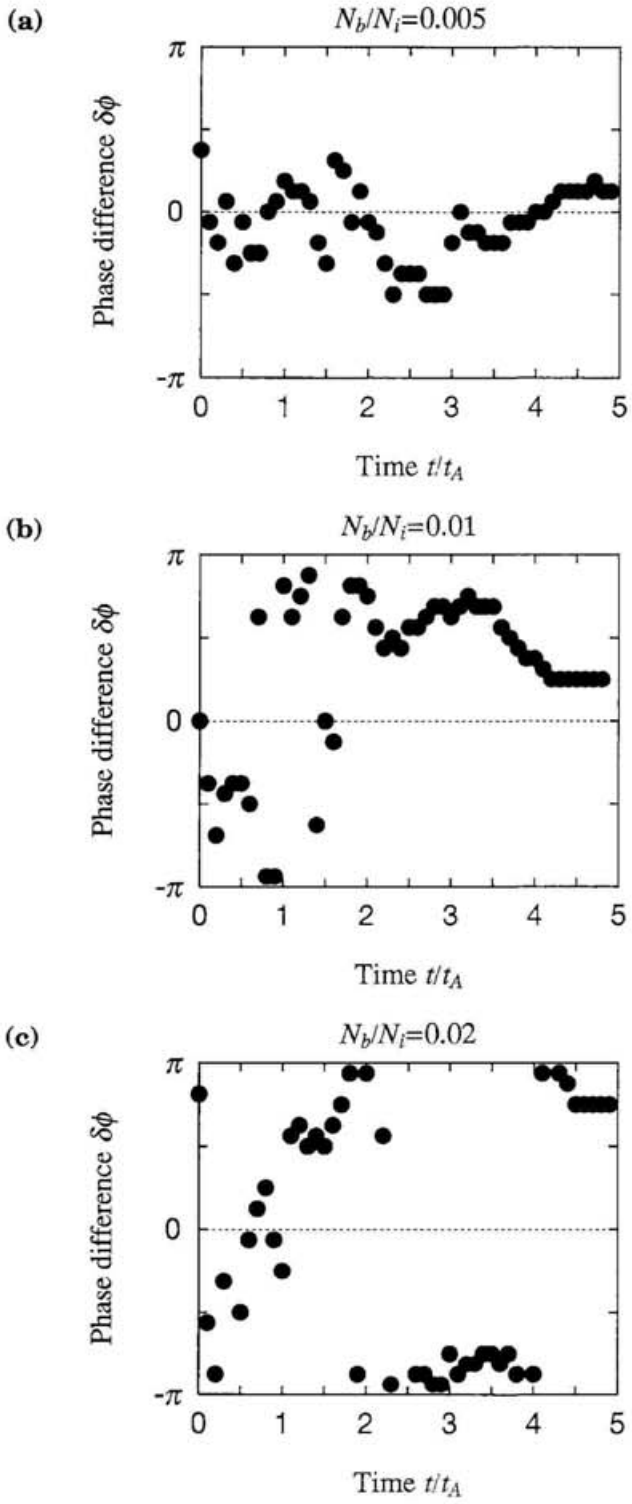

Figure 3.23: Time histories of phase difference between the tilt forces acting on thermal ions and beam ions for three different number ratios, i.e., (a) $N_b/N_i = 0.005$, (b) $N_b/N_i = 0.01$, and (c) $N_b/N_i = 0.02$.

Chapter 4

Conclusions

In order to investigate the tilt stabilization mechanism in FRC plasmas, we have developed a three-dimensional particle simulation code which can describe the finite ion Larmor radius effect, the profile control effect, and the ion beam effect simultaneously. By carrying out the simulation runs with controlling each effect independently, we obtained several new results as follows.

(1) We investigated both the finite ion Larmor radius effect and the profile control effect in the tilt stabilization for the case where no beam ion exists. The finite ion Larmor radius effect is characterized by the parameter $\bar{s}$ which is roughly the ratio of plasma radius to average ion gyroradius. The profile control effect is characterized by β_{sp} and D, where the parameter β_{sp} represents roughly the plasma beta value at the separatrix and D is the hollowness parameter which determines the current profile. By carrying out the simulation runs with different values of β_{sp}, $\bar{s}$, and D for a moderately kinetic plasma ($2 \leq \bar{s} \leq 5$), we have clarified that the tilt instability is effectively stabilized by increasing the separatrix beta value ($\beta_{sp} \geq 0.2$). On the other hand, the stabilization of tilt mode can be scarcely altered by changing the

parameter $\bar{s}$ and the current profile parameter D for low β_{sp} (≤ 0.1) and moderately kinetic plasmas.

(2) The detailed analysis reveals that the number flux of the ions crossing the magnetic separatrix repeatedly (cycling ions) increases in proportion to β_{sp} and the tilt stability is realized for a large number flux of cycling ions.

(3) The cycling ions play a role as "chain" to connect the internal plasma with the external plasma and stabilize the tilting motion through their "chain" effect. In order to elucidate the physical picture of "chain" effect, we investigated the force $(\boldsymbol{j} \times \boldsymbol{B})_z^{(1)}$ which generates the tilt motion along the z direction. The current density is expanded into the cycling component and the non-cycling component. For the unstable case, one component of the $\boldsymbol{j} \times \boldsymbol{B}$ force works synchronously on the plasma to the same direction as the other component so that the tilt instability grows swiftly on the whole. For the stable case, however, the amplitudes of two forces remain smaller than those for the unstable case and the phase difference is always large ($\delta\phi \sim \pm\pi$). It is concluded that the $\boldsymbol{j} \times \boldsymbol{B}$ force by the cycling ions works on the plasma so as to cancel the tilting force by the non-cycling ions.

(4) We investigated the ion beam effect for the case where the energetic ion beam is injected in the vicinity of field-null line of a tilt unstable profile ($\bar{s} = 3, \beta_{sp} = 0.02$, and $D = -0.6$). By carrying out the simulation runs with different values of I_b/I_p and N_b/N_i, it is found that the tilt growth rate remains almost unchanged until the current ratio reaches the critical value $R_c(\simeq 0.03)$, and then it gradually decreases as the ratio increases above R_c. The dependence of the growth rate on the current ratio I_b/I_p are exactly the same for both the fixed number case and the fixed velocity

case. That is to say, we can evaluate the ion beam effect universally with use of the current ratio.

(5) We can also evaluate the efficiency of the tilt stabilization by beam ions in terms of the kinetic energy. Comparing with the fixed number case and the fixed velocity case, we come to the conclusion that the tilt mode can be suppressed more effectively by increasing the number of beam ions. That is to say, in the case where the velocity of beam ions varies, the ion beam needs 30% of the kinetic energy of the thermal ions to reduce the growth rate below a half of that for no beam case. On the other hand, in the case where the total number of beam ions varies, only 15% of the kinetic energy of thermal ions is needed for beam ions to get the same growth rate.

Acknowledgement

I wish to express my gratitude to Professor Ritoku Horiuchi for his patient guidance and warm encouragement for two years.

I am indebted to Professor Tetsuya Sato for providing me with the opportunity to study plasma physics at National Institute for Fusion Science (NIFS).

I would like to thank Dr. Yukihiro Tomita for reading the entire manuscript in the original form of this thesis and making a number of helpful suggestions. I would like to thank Dr. Ryutaro Kanno for providing me with many valuable references and for helpful suggestions and comments. I gratefully acknowledge helpful and valuable comments by Professor Akio Ishida and Dr. Loren C. Steinhauer on Section 3.1 in this thesis. I would like to thank Dr. Yasushi Todo and Dr. Hisanori Takamaru for useful discussions and comments on particle simulation techniques for plasma physics. I would like to thank Dr. Tomohiko Watanabe for valuable discussions and critical comments through this investigation. Dr. Hideaki Kitauchi helped me in drawing several figures in this thesis. Thanks are due to all members of Theory and Computer Simulation Center of NIFS for their valuable advice and helpful supports.

The simulation work was performed by employing the Advanced Computing System for Complexity Simulation (NEC SX-3/24R) at NIFS.

Kazumi Nishimura

Bibliography

[1] H. P. Furth, "The compact torus, dense plasma in a theta pinch," *J. Vac. Sci. Technol.*, **18**, 1073-1080 (1981).

[2] T. Green, "Evidence for the containment of a hot, dense plasma in a theta pinch," *Phys. Rev. Lett.*, **5**, 297-300 (1960).

[3] A. G. Es'kov, R. Kh. Kurtmullaev, A. P. Kreshchuk, Ya. N. Laukhin, A. I. Malyutin, A. I. Markin, Yu. S. Martyushov, B. N. Mironov, M. M. Orlov, A. P. Proshletsov, V. N. Semenov, and Yu. B. Sosunov, "Principles of plasma heating and confinement in a compact toroidal configuration," in *Plasma Physics and Controlled Nuclear Fusion Research*, 1982 (IAEA, Vienna, 1983), Vol. I, pp.187-204.

[4] J. T. Slough, A. L. Hoffman, and R. D. Milroy, "Formation studies of field-reversed configurations in a slow field-reversed theta pinch," *Phys. Fluids*, B**1**, 840-850 (1989).

[5] J. T. Slough and A. L. Hoffman, "Experimental study of the formation of field-reversed configurations employing high-order multipole fields," *Phys. Fluids*, B**2**, 797-808 (1990).

[6] M. Tuszewski, W. T. Armstrong, R. E. Chrien, W. N. Hugrass, K. F. Mckenna, D. J. Rej, R. E. Siemon, D. P. Taggart, and B. L. Wright, "Axial dynamics in field-reversed

theta pinches. I: Formation," *Phys. Fluids*, B**3**, 2844-2855 (1991).

[7] W. T. Armstrong, R. K. Linford, J. Lipson, D. A. Platts, and E. G. Sherwood, "Field-reversed experiments (FRX) on compact toroids," *Phys. Fluids*, **24**, 2068-2089 (1981).

[8] H. Momota, A. Ishida, Y. Kohzaki, G. H. Miley, S. Ohi, M. Ohnishi, K. Sato, L. C. Steinhauer, Y. Tomita, and M. Tuszewski, "Conceptual design of the D-^{3}He reactor ARTEMIS," *Fusion technol.*, **21**, 2307-2323 (1992).

[9] H. Momota and Y. Tomita, "D-^{3}He fueled FRC power plant for the 21st century," *J. Plasma and Fusion Research*, **67**, 539-549 (1992).

[10] T. Takahashi, Y. Tomita, H. Momota, and N. V. Shabrov, "Collisionless pitch angle scattering of plasma ions at the edge region of a field-reversed configuration," *Phys. Plasmas*, **4**, December (1997).

[11] M. Tuszewski, "Field reversed configurations," *Nucl. Fusion*, **28**, 2033-2092 (1988).

[12] H. L. Berk, J. H. Hammer, and H. Weitzner, "Analytic field-reversed equilibria," *Phys. Fluids*, **24**, 1758-1759 (1981).

[13] R. L. Spencer and D. W. Hewett, "Free-boundary field-reversed configuration (FRC) equilibria in a conducting cylinder," *Phys. Fluids*, **25**, 1365-1369 (1982).

[14] R. B. Webster, J. L. Schwarzmeier, H. R. Lewis, C. K. Choi, and W. K. Terry, "Two-dimensional kinetic field-reversed equilibria," *Phys. Fluids*, B**3**, 1026-1040 (1991).

[15] D. W. Hewett and R. L. Spencer, "Two-dimensional equilibria of field-reversed configurations in a perfectly conducting cylindrical shell," *Phys. Fluids*, **26**, 1299-1304 (1983).

[16] S. Kaneko, K. Chiyoda, and I. Hirota, "Magnetohydrodynamic equilibrium with spheroidal plasma-vacuum interface – compact toroid without toroidal magnetic field –," *J. Phys. Soc. Jpn.*, **52**, 2016-2024 (1983).

[17] M. Kako, T. Ishimura, and T. Amano, "Equilibria of field-reversed configuration with subsidiary coils," *J. Phys. Soc. Jpn.*, **52**, 3056-3065 (1983).

[18] K. Suzuki, "Two dimensional field reversed equilibria with plasma outside the separatrix," *J. Phys. Soc. Jpn.*, **54**, 2155-2159 (1985).

[19] M. Tuszewski, "Experimental study of the equilibrium of field-reversed configurations," *Plasma Phys. Contr. Fusion*, **26**, 991-1005 (1984).

[20] R. L. Spencer and M. Tuszewski, "Experimental and computational equilibria of field-reversed configurations," *Phys. Fluids*, **28**, 1810-1815 (1985).

[21] S. Ohi, T. Minato, Y. Kawakami, M. Tanjyo, S. Okada, Y. Ito, M. Kako, S. Goto, T. Ishimura, and H. Ito, "Quadrupole stabilization of the $n = 2$ rotational instability of a field-reversed theta-pinch plasma," *Phys. Rev. Lett.*, **51**, 1042-1045 (1983).

[22] A. L. Hoffman, J. T. Slough, and D. G. Harding, "Suppression of the $n = 2$ rotational instability in field-reversed configurations," *Phys. Fluids*, **26**, 1626-1629 (1983).

[23] M. Ohnishi, H. Kuranaga, and M. Okamoto, "Suppression, by ion beams, of the $m = 2$ rotational instability in a field reversed configuration," *Nucl. Fusion*, **28**, 1427-1438 (1988).

[24] M. Ohnishi, A. Ishida, and T. Akasaka, "Ion beam stabilization of rotational instability in a field-reversed configuration with rigid rotation," *Phys. Fluids*, B**5**, 1842-1849 (1993).

[25] C. Bartoli and T. S. Green, "Flip instability of plasma in the theta pinch," *Nucl. Fusion*, **3**, 84-88 (1963).

[26] M. N. Rosenbluth and M. N. Bussac, "MHD stability of spheromak," *Nucl. Fusion*, **19**, 489-498 (1979).

[27] J. B. Taylor, "Relaxation of toroidal plasma and generation of reverse magnetic fields," *Phys. Rev. Lett.*, **33**, 1139-1141 (1974).

[28] R. A. Clemente and J. L. Milovich, "The tilting mode in field-reversed configurations," *Physics Letters*, **85A**, 148-150 (1981).

[29] G. Bateman, *MHD Instabilities,* MIT, Cambridge, Massachusetts (1978) p.92.

[30] I. B. Bernstein, E. A. Frieman, M. D. Kruskal, and R. M. Kulsrud, "An energy principle for hydromagnetic stability problems," *Proc. R. Soc. London Ser. A*, **244**, 17-40 (1958).

[31] R. A. Clemente and C. E. Grillo, "Internal tilting and classical transport for field-reversed configurations based on the Maschke-Hernegger solution," *Phys. Fluids*, **27**, 658-660 (1984).

[32] J. H. Hammer, "MHD tilting modes for nearly spherical compact toroids with arbitrary plasma pressure," *Nucl. Fusion*, **28**, 488-492 (1981).

[33] J. L. Schwarzmeier, D. C. Barnes, D. W. Hewett, C. E. Seyler, A. I. Shestakov, and R. L. Spencer, "Magnetohydrodynamic equilibrium and stability of field-reversed configurations," *Phys. Fluids*, **26**, 1295-1298 (1983).

[34] A. I. Shestakov, J. Killeen, and D. D. Schnack, "A numerical model for nonaxisymmetric MHD instabilities," *J. Comp. Phys.*, **46**, 69-96 (1982).

[35] R. Horiuchi and T. Sato, "Full magnetohydrodynamic simulation of the tilting instability in a field-reversed configuration," *Phys. Fluids*, B**1**, 581-590 (1989).

[36] R. D. Milroy, D. C. Barnes, R. C. Bishop, and R. B. Webster, "Nonlinear magnetohydrodynamic studies of the tilt mode in field-reversed configurations," *Phys. Fluids*, B**1**, 1225-1232 (1989).

[37] A. Ishida, H. Momota, and L. C. Steinhauer, "Variational formulation for a multifluid flowing plasma with application to the internal tilt mode of a field-reversed configuration," *Phys. Fluids*, **31**, 3024-3034 (1988).

[38] J. T. Slough, A. L. Hoffman, R. D. Milroy, D. G. Harding, and L. C. Steinhauer, "Flux and particle life-time measurements in field-reversed configurations," *Nucl. Fusion*, **24**, 1537-1550 (1984).

[39] J. P. Freidberg, "Vlasov-fluid model for studying gross stability of high-β plasmas," *Phys. Fluids*, **15**, 1102-1108 (1972).

[40] C. E. Seyler, Jr. and D. C. Barnes, "Finite Larmor radius model for axisymmetric compact toroids," *Phys. Fluids*, **24**, 1989-1998 (1981).

[41] H. R. Lewis, D. C. Barnes, J. L. Schwarzmeier, and C. E. Seyler, "The dispersion functional for multidimensional equilibria," *Phys. Fluids*, **28**, 3546-3556 (1985).

[42] D. C. Barnes, J. L. Schwarzmeier, H. R. Lewis, and C. E. Seyler, "Kinetic tilting stability of field-reversed configurations," *Phys. Fluids*, **29**, 2616-2629 (1986).

[43] J. L. Schwarzmeier and C. E. Seyler, "Inadequacies of finite Larmor radius treatments of the internal tilting instability in field-reversed configurations," *Phys. Fluids*, **27**, 2151-2155 (1984).

[44] R. Horiuchi and T. Sato, "The meandering orbit effect on stabilization of the tilting instability in a field-reversed configuration," *Phys. Fluids*, B**2**, 2652-2660 (1990).

[45] L. C. Steinhauer and A. Ishida, "Profile consistency in equilibria of field-reversed configurations," *Phys. Fluids*, B**4**, 645-650 (1992).

[46] J. W. Cobb, T. Tajima, and D. C. Barnes, "Profile stabilization of tilt mode in a field-reversed configuration," *Phys. Fluids*, B**5**, 3227-3238 (1993).

[47] L. C. Steinhauer, A. Ishida, and R. Kanno, "Ideal stability of a toroidal confinement system without a toroidal magnetic field," *Phys. Plasmas*, **1**, 1523-1528 (1994).

[48] R. Kanno, A. Ishida, and L. C. Steinhauer, "Ideal-magnetohydrodynamic-stable tilting in field-reversed configurations," *J. Phys. Soc. Jpn.*, **64**, 463-478 (1995).

[49] J. B. Taylor, "Rotation and instability of plasma in fast B_z compression experiments," *J. Nucl. Energy Part C*, **4**, 401-407 (1962).

[50] L. C. Steinhauer, "Plasma rotation in reversed-field theta pinches," *Phys. Fluids*, **24**, 328-338 (1981).

[51] M. Tuszewski, G. A. Barnes, R. E. Chrien, W. N. Hugrass, D. J. Rej, R. E. Siemon, and B. Wright, "The origin of the rotation in field-reversed configurations," *Phys. Fluids*, **31**, 946-948 (1988).

[52] R. A. Clemente and J. L. Milovich, "The tilting mode in rigidly rotating field-reversed configurations," *Phys. Fluids*, **26**, 1874-1876 (1983).

[53] H. L. Berk, "Effect of energetic particles on plasma stability," in *From Particles to Plasma*, edited by J. W. Van Dam, (Addison-Wesley Publishing Company, 1988) pp. 317-330.

[54] J. M. Finn and R. N. Sudan, "Field-reversed configurations with a component of energetic particles," *Nucl. Fusion*, **22**, 1443-1518 (1982).

[55] Y. Nomura, "Suppression of tilting instability of a compact torus by energetic particle beams," *J. Phys. Soc. Jpn.*, **54**, 1369-1379 (1985).

[56] D. C. Barnes and R. D. Milroy, "Stabilization of the field-reversed configuration (FRC) tilt instability with energetic ion beams," *Phys. Fluids*, B**3**, 2609-2616 (1991).

[57] J. T. Slough, A. L. Hoffman, R. D. Milroy, R. Maqueda, and L. C. Steinhauer, "Transport, energy balance, and stability of a large field-reversed configuration," *Phys. Plasmas*, **2**, 2286-2291 (1995).

[58] J. T. Slough, A. L. Hoffman, R. D. Milroy, E. A. Crawford, M. Cecik, R. Maqueda, G. A. Wurden, Y. Ito, and A. Shiokawa, "Confinement and stability of plasmas in a field-reversed configuration," *Phys. Rev. Lett.*, **69**, 2212-2215 (1992).

[59] A. L. Hoffman and J. T. Slough "Field reversed configuration lifetime scaling based on measurements from the large s experiment," *Nucl. Fusion*, **33**, 27-38 (1993).

[60] A. L. Hoffman, L. N. Carey, E. A. Crawford, D. G. Harding, T. E. Dehart, K. F. Mcdonald, J. L. Mcneil, R. D. Milroy, J. T. Slough, R. Maqueda, and G. A. Wurden, "The large-s field-reversed configuration experiment," *Fusion Technol.*, **23**, 185-207 (1993).

[61] J. T. Slough and A. L. Hoffman, "Stability of field-reversed configurations in the large s experiment (LSX)," *Phys. Fluids*, B**5**, 4366-4377 (1993).

[62] M. Tuszewski, D. C. Barnes, R. E. Chrien, J. W. Cobb, D. J. Rej, R. E. Siemon, D. P. Taggart, and B. L. Wright, "Observations of tilt instabilities in field-reversed configurations of a confined plasma," *Phys. Rev. Lett.*, **66**, 711-714 (1991).

[63] R. E. Siemon, R. E. Chrien, W. N. Hugrass, S. Okada, D. J. Rej, D. P. Taggart, M.Tuszewski, R. B. Webster, B. L. Wright, J. T. Slough, E. A. Crawford, Z. A. Pietrzyk, R. Raman, and R. Smith, "Field reversed configuration experiments," in *Plasma Physics and Controlled Nuclear Fusion Research, 1988*, Proceedings of the 12th International Conference, Nice (IAEA, Vienna, 1989), Vol. II, pp. 517-526.

[64] R. E. Siemon, W. T. Armstrong, D. C. Barnes, R. R. Bartsch, R. E. Chrien, J. C. Cochrane, W. N. Hugrass, R. W. Kewish, Jr., P. L. Klingner, H. R. Lewis, R. K. Linford, K. F. Mckenna, R. D. Milroy, D. J. Rej, J. L. Schwarzmeier, C. E. Seyler, E. G. Sherwood, R. L. Spencer, and M. Tuszewski, "Review of the Los Alamos FRX-C experiment," *Fusion Technol.*, **9**, 13-37 (1986).

[65] M. Tuszewski, D. P. Taggart, R. E. Chrien, D. J. Rej, R. E. Siemon, and B. L. Wright, "Axial dynamics in field-reversed theta pinches. II: Stability," *Phys. Fluids*, B**3**, 2856-2870 (1991).

[66] J. L. Johnson, H. E. Dalhed, J. M. Greene, R. C. Grimm, Y. Y. Hsieh, S. C. Jardin, J. Manickam, M. Okabayashi, R. G. Storer, A. M. M. Todd, D. E. Voss, and K. E. Weimer, "Numerical determination of axisymmetric toroidal magnetohydrodynamic equilibria," *J. Comput. Phys.*, **32**, 212-234 (1979).

[67] C. K. Birdsall and A. B. Langdon, *Plasma Physics Via Computer Simulation* (McGraw-Hill, New York, 1985) p.168.

[68] R. Horiuchi and T. Sato, "Particle simulation study of driven magnetic reconnection in a collisionless plasma," *Phys. Plasmas*, **1**, 3587-3597 (1994).

[69] M. Tanaka and T. Sato "Macroscale particle simulation of relativistic electron beam injection into a magnetized plasma channel," *Phys. Fluids*, **29**, 3823-3831 (1986).

[70] R. Courant, K. O. Friedriches, and H. Lewy, "Über die partiellen Differenzengleichungen der mathematischen Physik," *Math. Ann.*, **100**, 32-74 (1928).

[71] K. Nishimura, R. Horiuchi, and T. Sato, "Tilt stabilization by cycling ions crossing magnetic separatrix in a field-reversed configuration," *Phys. Plasmas*, **4**, 4035-4042 (1997).